Materials Today Bio 17 (2022) 100485

Contents lists available at ScienceDirect

Materials Today Bio

journal homepage: www.journals.elsevier.com/materials-today-bio

An all-silk-derived bilayer hydrogel for osteochondral tissue engineering

Weizhou Jiang [a,1], Xiuting Xiang [b,1], Minkai Song [a], Jianlin Shen [c], Zhanjun Shi [a,**], Wenhua Huang [d,e,***], Huan Liu [f,*]

[a] Department of Orthopaedics, Nanfang Hospital, Southern Medical University, Guangzhou, 510515, China
[b] Department of Biomedical Science, Faculty of Medicine and Health Sciences, University Malaysia Sabah, Kota Kinabalu, 88999, Malaysia
[c] Department of Orthopedics, Affiliated Hospital of Putian University, Putian, 351106, China
[d] Guangdong Medical Innovation Platform for Translation of 3D Printing Application, The Third Affiliated Hospital of Southern Medical University, Southern Medical University, Guangzhou, 510515, China
[e] Guangdong Engineering Research Center for Translation of Medical 3D Printing Application, Guangdong Provincial Key Laboratory of Medical Biomechanics, School of Basic Medical Sciences, Southern Medical University, Guangzhou 510515, China
[f] Department of Orthopedics, The Affiliated Traditional Chinese Medicine Hospital of Southwest Medical University, Luzhou, 646000, China

ARTICLE INFO

Keywords:
Osteoarthritis
Osteochondral defect
Silk fibroin
Drug-loaded microsphere
Tissue engineering

ABSTRACT

Osteochondral repair remains a challenge in clinical practice nowadays despite extensive advances in tissue engineering. The insufficient recruitment of endogenous cells in the early stage and incomplete cell differentiation in the later stage constitute the major difficulty of osteochondral repair. Here, a novel all-silk-derived multifunctional biomaterial platform for osteochondral engineering is reported. The bilayer methacrylated silk fibroin (SilMA) hydrogel was fabricated through stratified photocuring as the basic provisional matrix for tissue regeneration. Platelet-rich plasma (PRP) incorporation promoted the migration and pre-differentiation of the bone marrow mesenchymal stem cells (BMSCs) in the early stage of implantation. The long-term regulation of BMSCs chondrogenesis and osteogenesis was realized by the stratified anchoring of the silk fibroin (SF) microspheres respectively loaded with Kartogenin (KGN) and berberine (BBR) in the hydrogel. The composite hydrogels were further demonstrated to promote BMSCs chondrogenic and osteogenic differentiation under an inflammatory microenvironment and to achieve satisfying cartilage and subchondral bone regeneration with great biocompatibility after 8 weeks of implantation. Since all the components used are readily available and biocompatible and can be efficiently integrated via a simple process, this composite hydrogel scaffold has tremendous potential for clinical use in osteochondral regeneration.

1. Introduction

Articular cartilage lacks the innate self-repair capability, thus even small and superficial defects fail to heal without cells and factors conducive to healing [1]. At present, traditional clinical techniques for cartilage repair, including marrow stimulation, allografts and autografts, have achieved limited success, but each of them remains its own popularization challenges [2–6]. Overall, the current therapies for hyaline cartilage regeneration are essentially failed. Irreparable cartilage damage can further expand and develop involving the subchondral bone, leading to the progression of osteoarthritis (OA) and ultimately the breakdown of the whole joint [7]. As the only option for end-stage OA treatment, total joint replacement, which reconstructs a painless joint with implantation of non-degradable metal and plastic materials, is actually more of a compromise than a solution [8]. Patients are at the risk of prosthesis wear, loosening, dislocation and infection after surgery for a lifelong time, thus this technique is unsuitable for the young population. Regeneration of early-stage osteochondral lesions stands for a more compelling academic and clinical goal.

Great efforts in the fields of tissue engineering and developmental biology have been dedicated to the understanding of physiological cues needed for osteochondral tissue regeneration [9]. Numerous

* Corresponding author.
** Corresponding author.
*** Corresponding author. Guangdong Engineering Research Center for Translation of Medical 3D Printing Application, Guangdong Provincial Key Laboratory of Medical Biomechanics, School of Basic Medical Sciences, Southern Medical University, Guangzhou, 510515, China.
E-mail addresses: orthopshi@163.com (Z. Shi), huangwenhua2009@139.com (W. Huang), 20016040@163.com (H. Liu).
[1] Wenzhou Jiang and Xiutang Xiang contributed equally to this work.

https://doi.org/10.1016/j.mtbio.2022.100485
Received 17 September 2022; Received in revised form 29 October 2022; Accepted 1 November 2022
Available online xxxx

encouraging laboratory advances in osteochondral engineering have achieved, though the clinical translation is rare [10,11]. The gaps between academic progress and clinical adoption are the key characteristics of several laboratory techniques, such as system simplicity, versatility, reproducibility and scalability, hard to meet the high-throughput manufacture required for translational applications. Especially, all of those techniques involving cell manipulation and delivery, with or without the use of biomaterials, are difficult and costly. Thus, the strategy of cell-free and biodegradable scaffolds implantation combined with microfracture technology, which promotes the recruitment of endogenous cells, is more in line with the requirement of clinical translation [10,12]. However, problems such as incomplete integration with native tissue and unsatisfactory quality of regenerated tissue remain to be solved in the recent clinical trials of several commercialized synthetic cell-free scaffolds [13–15]. It suggests that more biophysical and biochemical clues, guiding the physiological process of regeneration of endogenous cells, should be effectively integrated into the biomaterials to pursue a more elegant balance between the simplicity and efficacy of osteochondral engineering scaffolds.

Silk fibroin (SF), a U.S. Food and Drug Administration (FDA) approved biomaterial for clinical use, has been widely used in osteochondral engineering due to its attractive properties [16,17]. Recently, a novel silk-modified biomaterial, methacrylated SF (SilMA), has been fabricated through the addition of methacrylate groups to amine residues of SF [18]. SilMA can be rapidly photocured into hydrogel formation, whose many critical properties are advantageous in osteochondral regeneration, including editable mechanical stiffness, elasticity, water content and bioactivity, while retaining good biocompatibility, strong mechanical properties and slow but completely biodegradable properties of SF molecules [19]. Park et al. realized cartilage tissue formation in rabbit trachea through the transplantation with chondrocytes-laden SilMA by 3D Digital Lighting Processing (DLP) printing [20]. The 3D-printable property of SilMA preserves a chance to further enhance the efficacy of hydrogel scaffolds by printing internal structures, despite that which structure is most conducive to osteochondral regeneration remains controversial. In addition, SilMA hydrogels showed tremendous potential in solving the lateral integration of adjoining tissue and implanted scaffold [21].

The recruitment, proliferation and differentiation of endogenous cells are critical to cell-free scaffolds [12]. As a cost-effective and readily available autologous biomaterial, platelet-rich plasma (PRP) seems to be an attractive candidate for incorporation into the scaffold due to its properties of promoting migration, proliferation, chondrogenic and osteogenic differentiation of bone marrow mesenchymal stem cells (BMSCs) [22]. However, due to the bioactive ingredients of PRP are protein molecules, it is vulnerable to being quickly deactivated by enzymatic degradation in joints. Integration of signaling molecules with a more stable structure into the regeneration system to ensure the long-term regulation of BMSCs differentiation should be considered. Kartogenin (KGN) has been well-recognized to induce BMSCs

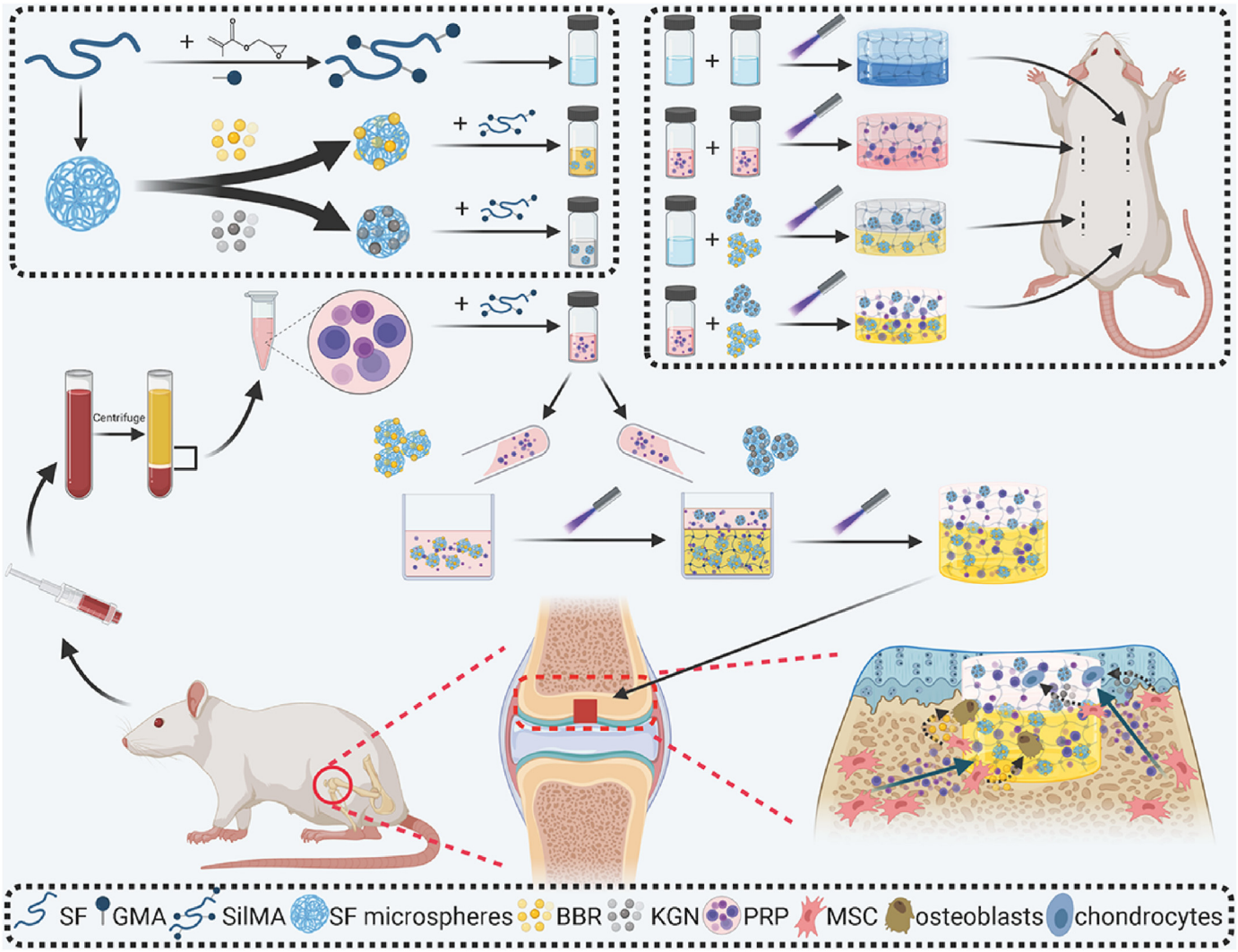

Fig. 1. Overview of the integral bilayer SilMA hydrogel scaffold combined with PRP and the SF-KGN and SF-BBR microspheres in osteochondral repair.

chondrogenesis and promote cartilage repair in a dose-dependent manner *in vitro* and *in vivo*, and has been applied in osteochondral engineering in various forms [23–26]. Berberine (BBR) has been reported to induce BMSCs osteogenesis and inhibit OA progression in animal models [27–30]. Moreover, the antioxidant and anti-inflammatory properties of BBR are expected to inhibit oxidative stress-induced apoptosis and maintain the differentiation potentials of BMSCs under the inflammatory environment of injured joints [31,32]. Besides, the hydrophobicity of KGN and BBR allows them to be efficiently encapsulated in SF nano- and microspheres using a simple, rapid and scalable method described by Wang et al., thereby realizing long-term sustained release [33,34].

In the present study, an all-silk-derived multifunctional biomaterial platform was proposed for osteochondral engineering (Fig. 1). We evaluated the physicochemical and biological properties of the composite scaffolds *in vitro*, and demonstrated those incorporated signaling molecules can promote the chondrogenic and osteogenic differentiation of BMSCs under an inflammatory microenvironment. Furthermore, the composite scaffolds were implanted into osteochondral defects to explore their functional outcomes and biocompatibility in a rat model.

2. Materials and methods

2.1. Preparation of SF solution and SilMA hydrogel

SF solution at the concentration of approximate 8% (w/v) was prepared as previously reported [35]. To obtain the concentrated SF solution, the 8% SF solution was further dialyzed against 10% (w/v) polyethylene glycol (PEG) (10,000 MW) solution for certain hours and then diluted with ultrapure water to obtain desired concentrations.

SilMA was prepared as previously reported [18]. Briefly, after the SF was dissolved by lithium bromide (LiBr), glycidyl methacrylate (GMA) solution (Sigma-Aldrich, St. Louis, USA) was added to the mixture with stirring at 300 rpm for 3 h at 60 °C. Then, the resulting solution was dialyzed against ultrapure water, followed by a freeze-dried procedure. For preparing SilMA hydrogels, lyophilized SilMA was dissolved in PBS at 10%, 20% and 30% (w/v), and the photoinitiator lithium phenyl(2,4,6-trimethylbenzoyl) phosphinate (LAP) (Sigma-Aldrich, St. Louis, USA) was added into the mixture at 0.2%. The prepared SilMA/LAP solution was photocrosslinked by exposure to 30 mW/cm^2 ultraviolet (UV) light.

2.2. Preparation of SF nano- and microspheres, and drug-loaded SF microspheres

SF nano- and microspheres were prepared as previously reported [33]. Briefly, SF solution with concentrations of 1%, 5%, 10% and 20% was mixed with 50% (w/v) PEG (10,000 MW) solution at a volume ratio of 1/1, and the mixture was pipetted dropwise into stirring anhydrous ethanol solution at a volume ratio of 1:5. The solution was incubated for 24 h at room temperature, followed by the processes of centrifugation and resuspension to remove the PEG and ethanol. To fabricate the drug-loaded microspheres, 2.5 mg of BBR or KGN were dissolved in 0.5 mL of 50% (w/v) PEG (10,000 MW) solution and then mixed with 0.5 mL of 10% SF solution. The rest steps were the same as described above. The washed nano- and microspheres were lyophilized and stored at 4 °C in a sealed container before use.

2.3. Extraction of PRP and BMSCs

The animals used in this research were provided by the Putian University Animal Center (Putian, China). All animal protocols were approved by the Animal Care and Experiment Committee of the Putian University.

PRP was prepared as previously reported [36]. Briefly, whole blood for PRP preparation was collected from the cardiac tissue of adult Sprague Dawley (SD) rats. The blood sample was centrifuged at 200 g for 30 min, followed by the transfer of the supernatant platelets to another tube. Then the second centrifugation at 2000*g* for 10 min was performed to enrich the platelets. The obtained unactivated PRP sample was further activated through the addition of thrombin at a ratio of 1/9. After incubation overnight at 4 °C, the percolate was collected as activated PRP and then stored at −80 °C until further use.

BMSCs were extracted from the femurs and tibias of neonatal SD rats. After flushing with the culture medium repeatedly, the bone marrow suspension was then transferred into the culture dish. The culture medium was replaced every 2 d until approximately 80% confluence was achieved. BMSCs at passages 3–5 were used for the *in vitro* experiments in this study.

2.4. Fabrication of composite-reinforced SilMA hydrogel scaffolds

The composite bilayer SilMA hydrogel scaffolds were fabricated as follows. First, the 30% SilMA solution was sterilized at 60 °C for 30 min; activated PRP was sterilized by using a 0.22 μm filter; SF-BBR and SF-KGN microspheres were sterilized using UV irradiation. SF-BBR and SF-KGN microspheres were respectively suspended by 30% SilMA solution to obtain S + B and S + K solution; the activated PRP was mixed with 30% SilMA solution at the concentrations of 1%, 5%, 10% and 20% to obtain S+1 P, S+5 P, S+10 P (S + P) and S+20 P solutions, respectively; SF-BBR and SF-KGN microspheres were respectively suspended by S + P solution to obtain S + B + P and S + K + P solution. The prepared solutions above were photocrosslinked by UV light for 1 min to obtain S + B, S + K, S+1 P, S+5 P, S+10 P (S + P), S+20 P, S + B + P and S + K + P hydrogels, respectively. The bilayer S hydrogel was obtained by adding 30% SilMA solution, which accounts for three-quarters of the final volume, in the silicone mold for 30 s photocuring, followed by adding the remaining quarter of 30% SilMA solution on the top of that for another 1 min photocuring. The S + P, S + B + K and S + B + K + P hydrogels were obtained in the same way (noted that the S + B and S + B + P solutions were added first when fabricating the S + B + K and S + B + K + P hydrogels).

2.5. Characterizations

To evaluate the microstructures of the SF nano- and microspheres and the hydrogel samples, a scanning electron microscope (SEM) (Carl-Zeiss, Oberkochen, Germany) was performed. The hydrodynamic size of the SF nano- and microspheres was determined using the dynamic light scattering (DLS) technique with a Zetasizer Nano S90 (Malvern, Worcestershire, UK) and a Mastersizer 2000 (Malvern, Worcestershire, UK), respectively. The surface zeta potential of the SF nano- and microspheres was determined using the Zetasizer Nano S90 (Malvern, Worcestershire, UK). The secondary structures of SF, SilMA, SF nano- and microspheres were confirmed by Fourier-transform infrared spectroscopy (FTIR) spectra using a Nicolet 5700 Spectrophotometer (Thermo, Massachusetts, USA) and by proton nuclear magnetic resonance (^{1}H NMR) at a frequency of 600 MHz using a Bruker DPX FT-NMR spectrometer (9.4 T, Bruker, Germany).

The swelling ratio of hydrogels was estimated using the method as previously [37]. Briefly, hydrogels were hydrated in PBS (pH 7.4) at 37 °C for 24 h, and the wet weight of the hydrogels (W1) was measured. Then the hydrogels were lyophilized and measured the dried weight (W0). The swelling ratio was calculated as follows: (W1 − W0)/W0 × 100%. The compressive stress-strain curves of hydrogels were obtained by applying uniaxial compression force with a universal testing machine (BOSEElectroForce 3220, Massachusetts, USA). A compression force was loaded at a displacement rate of 1 mm/min until the hydrogel disks with dimensions of 10 mm (diameter) and 10 mm (height) broke. From the stress-strain curve, the secant modulus at 5%, 20%, and 40% strain for the compressive test was calculated. For *in vitro* degradation test, hydrogel samples were incubated in PBS at 37 °C with shaking. The weight of the hydrogels at the beginning of the assay (Wt) and the

remaining weight of the hydrogels at the designated time points (Wr) were determined. The remaining mass was calculated as follows: Wr/Wt × 100%. Subcutaneous implantation in rats was performed to determine the *in vivo* biocompatibility of the hydrogels. The inflammatory response was examined by staining the tissue sections at 2 weeks post-implantation with hematoxylin & eosin (H&E) and Masson's trichrome (M&T) staining.

PRP is a plentiful source of growth factors. Platelet-derived growth factor (PDGF-AB) and transforming growth factor β1 (TGF-β1) were taken as representative cytokines and their concentrations in PRP were detected using ELISA kit (Wellbio, Shanghai, CN). For *in vitro* release studies, S + P and S + B + K + P hydrogels were fabricated and incubated in PBS at 37 °C with shaking. At the designated time points, supernatant fluid was collected for analysis and fresh PBS was refilled, and the cumulative releases of PDGF-AB and TGF-β1 from different hydrogels were calculated.

To determine the loading and encapsulation efficiency of BBR and KGN in the SF microspheres, the supernatant obtained from the washing steps of the drug-loaded microsphere was collected and the amount of BBR and KGN was determined using UV–VIS spectroscopy with a spectrophotometer (SP–2100UVPC, China). Absorbance values were taken at wavelengths of 349 nm and 273 nm, at which the BBR and KGN showed the absorbance maximum, respectively. Drug loading rate of SF microspheres was calculated as follows: amount of drug in SF microspheres/total amount of drug-loaded SF microspheres; encapsulation efficiency of SF microspheres was calculated as follows: amount of drug in SF microspheres/initial amount of drug added into SF solution. For *in vitro* release studies, BBR and KGN were added to the 30% SilMA solution at a concentration of 0.5 mg/mL, followed by a photocuring process to form SilMA + BBR and SilMA + KGN hydrogels. SF-BBR and SF-KGN microspheres were suspended in 30% SilMA solution at a concentration of 10 mg/mL, followed by a photocuring process to form SilMA + BBRms and SilMA + KGNms hydrogels. Then the above hydrogels were incubated in PBS at 37 °C with shaking. At the designated time points, supernatant fluid was collected for analysis and fresh PBS was refilled, and the cumulative releases of BBR and KGN from different hydrogels were calculated.

2.6. In vitro functional assessments of scaffold bioactive compositions

2.6.1. Cell proliferation

BMSCs were seeded on 30% SilMA, S + B, S + K, S + P, S + B + P and S + K + P hydrogels and cultured for 3 days. The cell-seeded hydrogel was washed with PBS, transferred to a new well, and incubated in 10% CCK-8 reagent (Dojindo Molecular, Japan) at 37 °C for 2 h. The absorbance was measured using a microplate reader (Thermo, Massachusetts, USA) at 450 nm.

2.6.2. Cell migration

The effect of the PRP on BMSCs migration was determined using the 24-well specific plates (5.0 μm) for Transwell assay. BMSCs were starved 24 h in advance to eliminate the influence of cell proliferation on experimental results. First, 500 μl of serum-free DMEM medium and the conditioned medium containing 1%, 5%, 10% and 20% PRP were added to 24-well plates. Subsequently, approximately 2×10^4 cells were seeded into the upper chamber of the Transwell plates and co-cultured with different mediums for 6 h. Next, 150 μl 30% SilMA, S+1 P, S+5 P, S+10 P, S+20 P, S + B, S + K, S + B + P and S + K + P hydrogels were placed into 24-well plates, followed by seeding approximately 2×10^4 cells into the upper chamber of the Transwell plates and co-cultured for 24 h. Finally, the number of cells was counted after crystal violet staining and used for comparison.

2.6.3. Chondrogenic and osteogenic differentiation

KGN was added to the chondrogenic conductive medium (without TGF-β) at a concentration of 10 μM to induce BMSCs chondrogenic differentiation. BBR was added to the osteogenic differentiation medium at concentrations of 1, 5 and 10 μM to induce BMSCs osteogenic differentiation. Next, BMSCs were seeded on S + K and S + B hydrogels and cultured in a chondrogenic conductive medium and osteogenic differentiation medium, respectively. BMSCs cultured in the same medium without KGN and BBR, and BMSCs seeded on SilMA hydrogel were used as controls. The gene expression of *Sox9*, *Acan* (aggrecan), *Col2a1* (collagen type II) and of *Runx2* (runt-related transcription factor 2), *Ocn* (osteocalcin), *Alp* (alkaline phosphatase) and *Bmp2* (bone morphogenetic protein 2) was examined using q-PCR analysis with the house-keeping gene Gapdh for normalization. The final results were determined using the 2-ΔΔCt method for relative gene expression. The sequences are listed in the supporting information (Table S1). Positive induction of osteogenesis was further confirmed by ALP staining.

2.6.4. LPS-induced inflammation

BMSCs were treated with Lipopolysaccharide (LPS, Sigma-Aldrich, St. Louis, USA) at 1 μg/mL for 6 h, 12 h, 24 h and 48 h to induce inflammation. The presence of the tumor necrosis factor (TNF)-α and interleukin (IL)-1β, in the supernatants was detected using ELISA kits (Elabscience Biotechnology Co., Wuhan, China) according to the manufacturer's instructions.

2.6.5. Chondrogenic and osteogenic differentiation under inflammatory conditions

The S, S + K, S + P and S + K + P hydrogels were prepared in 6-well plates, then the chondrogenic conductive medium of 5 times hydrogel volume was added and incubated in a 5% CO_2 incubator at 37 °C. Similarly, the S, S + B, S + P and S + B + P hydrogels were prepared and incubated using the osteogenic differentiation medium. The conditioned medium was extracted and sterilely filtered with the 0.2 μm filter for every 72 h. Then LPS was added to the conditioned medium at a concentration of 1 μg/mL. BMSCs were cultured in the above medium and the medium was changed every 3 days. Positive induction of chondrogenesis was confirmed by Alcin blue staining, and that of osteogenesis was confirmed by ALP staining. After induction, BMSCs were dissolved in RIPA buffer to extract the whole-tissue protein. The expression of chondrogenic markers (COL2 and SOX9) and osteogenic markers (RUNX2 and OPN) were detected by western blotting (WB) assays.

2.7. In vivo regeneration of osteochondral defects

Male SD rats (n = 40) with a mean weight of 120 g were randomly divided into four groups: S group, S + P group, S + B + K group and S + B + K + P group. After anesthesia via intraperitoneal injection of 3% pentobarbital sodium (30 mg/kg), a full-thickness osteochondral defect (diameter of 2 mm, depth of 2 mm) was made in the articular surface of the femoral patellar groove. Then, the composite bilayer scaffold (diameter of 2 mm, height of 2 mm) was implanted into the defect. The knee joint capsule and skin were sutured and disinfected. The rats were allowed to move freely within the cages. After 4 and 8 weeks of implantation, the rats were sacrificed to obtain knee, heart, liver, spleen, lung and kidney specimens for further assessment.

The fixed knee specimens at 4 and 8 weeks were photographed. Then, the micro-CT (l-CT 80 scanner, Scanco Medical, Bassersdorf, Switzerland) scan was conducted to evaluate the bone formation. For quantification of bone mineral density (BMD), bone volume/tissue volume (BV/TV), trabecular number (Tb. N), trabecular thickness (Tb. Th) and trabecular separation (Tb. Sp), a cylindrical area, whose radius are in the center of the defect site, was selected as the region of interest (ROI). After decalcification, dehydration, and embedding in paraffin, the knee specimens at 4 and 8 weeks were sliced and stained with H&E and Safranin-O fast green (Saf-O) staining. Afterward, the cartilage regeneration was graded blindly by two independent observers according to the international cartilage repair society (ICRS) scoring system [38,39]. Immunohistochemical staining for Collagen II (Abcam, UK) and CD 44

(Bioss, CN) was performed to evaluate the expression of cartilage marker and BMSCs marker, respectively. For *in vivo* biocompatibility evaluation, the heart, liver, spleen, lung and kidney specimens of all the experimental groups at 8 weeks and those of the normal SD rats were sliced and stained with H&E staining.

2.8. Statistical analysis

All statistical analyses were performed using a SPSS software v19.0 (IBM, NY, USA). The quantitative data are presented as mean ± standard deviation (SD). A comparison between two groups was performed using the student's t-test. Comparison for more than two groups was performed using the one-way ANOVA with Tukey's multiple comparisons. The levels of significance were established at $^{*}P < 0.05$, $^{**}P < 0.01$ and $^{***}P < 0.001$. ns denoted not significantly different.

3. Results and discussion

3.1. Fabrication and characterization of components of the composite scaffold

The good biocompatibility, robust mechanical properties, controllable degradability and easily modifiable properties into different material formats of SF constitute the structural and functional foundation of composite scaffolds [16,17,40]. The successful extraction of SF and fabrication of SilMA were confirmed through the identification of GMA-related peaks and SF-related peaks both in FTIR and ^{1}H NMR spectroscopy (Figs. S1A and B), which are consistent with the previous study [18]. The SEM images of SilMA hydrogels revealed uniform and interconnected porous microstructures (Fig. 2A, B, C), which facilitate cell adhesion and proliferation and the transfer of nutrients and signaling factors between cells. With the increase of SilMA concentration from 10% to 30%, the pore size showed decreasing pattern and the network fibers became thicker. The change of hydrogel structure is accompanied by the change of its physical properties. 30% SilMA hydrogels showed the lowest swelling ratio and the highest compressive elastic moduli (Fig. 2D and E). During the 30-day *in vitro* degradation, 30% SilMA hydrogels remained structurally intact and presented a smooth and slowest degradation profile (Fig. 2F). Considering that a stiffer matrix serves as a physical clue conducive to BMSCs chondrogenesis and osteogenesis [41], and the slowest degradation profile can provide long-term *in situ* stability after implantation, the 30% SilMA hydrogel was chosen for the subsequent research.

SF nano- and microspheres were fabricated as another key building block of the composite scaffold for the controlled release of biomolecules. By simply changing the concentration of SF solution from 1% to 20%, the sizes of spherical particles increased from tens of nanometers to tens of micrometers (Fig. 2G-R). The addition of ethanol after microsphere formation increased β-sheet and silk II structure (high crystallinity) of the microspheres, which were confirmed by FTIR tests (Fig. 2S). The surface zeta potential for the SF nano- and microspheres was about −18 mV (Fig. 2T), which enables the charge repulsion between spheres. The particle sizes did not significantly affect the surface zeta potentials, but the drug release patterns. The larger microspheres release drugs more slowly due to the lower surface-to-volume ratio and longer diffusion distance [33]. Besides, the larger microspheres are more resistant to cell internalization [42,43]. As microspheres of different sizes have different drug release rates and different interaction patterns with cells, the delivery way and temporal control of biochemical cues are possible to further optimize by adjusting the microspheres combination. In this study, we chose the 10% SF microspheres for the subsequent research due to their best roundness and homogeneousness, and relatively narrower particle size distribution (Fig. 2 K, L, Q). A previous study has shown that octreotide encapsulated in the 10% SF microspheres through the same method can release in a linear and sustained pattern over 102 days, which is sufficient to cover the whole osteochondral regeneration period [34].

SF microspheres can encapsulate both hydrophilic and hydrophobic molecules for the amphiphilic nature of SF [44]. Despite that, the hydrophobic interactions between SF and hydrophobic molecules, such as KGN and BBR, lead to higher binding affinity than that of hydrophilic molecules [45]. The SEM images and DLS measurements indicated that the SF-KGN and SF-BBR microspheres have similar particle sizes and narrow size distributions as the unloaded 10% SF microspheres (Fig. 3A–H). High magnification images revealed grains on the surface of SF-KGN and SF-BBR microspheres (Fig. 3C, F), suggesting the successful loading of KGN and BBR molecules on the SF microspheres. The surface zeta potentials for SF-KGN and SF-BBR microspheres were lower than that of the unloaded 10% SF microspheres (Fig. 3I). We speculate that the denser adsorption of drug molecules on the surface of microspheres and the less negative surface zeta potential for the SF-BBR microspheres might attribute to the stronger binding of BBR (positive charge) to SF microspheres via electrostatic attraction [46]. Similar to the unloaded SF microspheres, the secondary structures of SF-KGN and SF-BBR microspheres were dominated by the silk II structure (Fig. 3J). In this study, KGN and BBR were both added to the SF solution at a drug/silk weight ratio of 1/20. The drug loading rates of SF-KGN and SF-BBR microspheres were 3.16% and 4.31%, respectively. The encapsulation efficiency of SF-KGN and SF-BBR microspheres were 42.92% and 54.80%, respectively. The drug loading rates and encapsulation efficiency of SF-BBR microspheres were higher than those of the SF-KGN microspheres, which are consistent with the results of SEM observations and surface zeta potential tests discussed above. The relatively low encapsulation efficiencies of both SF-KGN and SF-BBR microspheres were likely due to the large volume of ethanol used, leading part of drug molecules to dissolve into ethanol. It is reported that ethanol treatment increased the β-sheet content of the SF microspheres, leading to a denser appearance and a significant reduction of drug burst release [34]. In order to obtain a better drug delivery system in line with application expectations, the encapsulation efficiency was compromised during the fabricating process.

For preparing the last bioactivate component of the scaffold, unactivated PRP was obtained with the method described by Landersberg [36], and then activated through thrombin addition (Fig. S2A). At present, there is no standardized protocol for PRP preparation [47]. The main criterion for successful PRP preparation is that the platelet count of PRP is 4–6 folds higher than that of the whole blood [48]. In this study, the mean platelet count of whole blood was 478.75 ± 85.00 ($\times 10^{9}$/L), while that of the PRP sample was 3229.50 ± 398.59 ($\times 10^{9}$/L) (Fig. S2B). The platelet enrichment coefficient was 6.82 ± 0.43, suggesting the successful PRP preparation. And after activation, representative growth factors, including PDGF-AB and TGF-β1, exhibited high concentrations in PRP (Fig. S2C).

3.2. Fabrication and characterization of the composite hydrogel scaffolds

Bilayer hydrogel scaffolds with different functional enhancements were obtained through different integration of the components above (Fig. 1). As observed by SEM, the pore surface of S + P hydrogel was rougher than that of the S hydrogel (Figs. S3A–D), indicating that protein molecules in PRP adhered to the pore surface of SilMA hydrogel. Similarly, the S + B + K + P hydrogel also revealed a rough pore surface (Fig. 4G and H), while that of S + B/S + K hydrogel looked smooth (Fig. 4A, B, D, E). Since PRP was directly mixed with SilMA solution, the growth factors (PDGF-AB and TGF-β1) from S + P hydrogels were mostly released in the first 10 days, and the release rates obviously slowed down afterward (Figs. S3E and F). The release kinetics of PDGF-AB and TGF-β1from S + B + K + P hydrogels were similar to those from S + P hydrogels (Figs. S3E and F). The quickly release of PDGF-AB and TGF-β1 ensured the promoting effect of PRP-incorporated hydrogels on the migration and pre-differentiation of the endogenous BMSCs at the early stage of implantation [49]. SF microspheres were obviously identified in

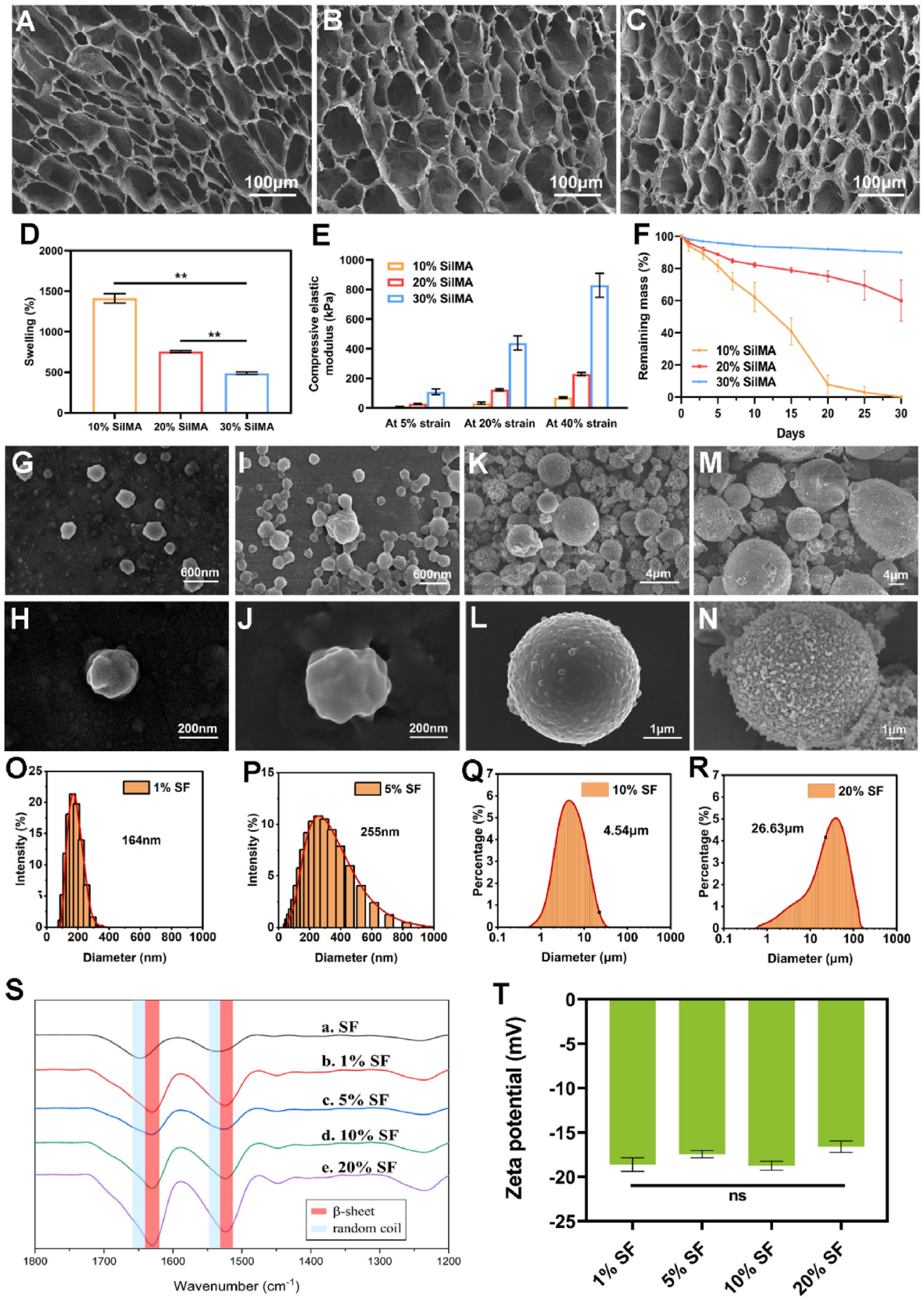

Fig. 2. SEM images of the 10% (A), 20% (B) and 30% SilMA hydrogels (C). Swelling ratio (D), compressive elastic modulus (E) and *in vitro* degradation profile (F) of the 10%, 20% and 30% SilMA hydrogels. Characterization of the SF nano- and microspheres. SEM images of the unloaded 1% SF nanospheres (G, H), unloaded 5% SF nanospheres (I, J), unloaded 10% SF microspheres (K, L), unloaded 20% SF microspheres (M, N). DLS measurements for the unloaded 1% SF nanospheres (O), unloaded 5% SF nanospheres (P), unloaded 10% SF microspheres (Q), unloaded 20% SF microspheres (R). FTIR spectra (S) and Zeta potential (T) of the SF nano- and microspheres. **P < 0.01. ns means P > 0.05.

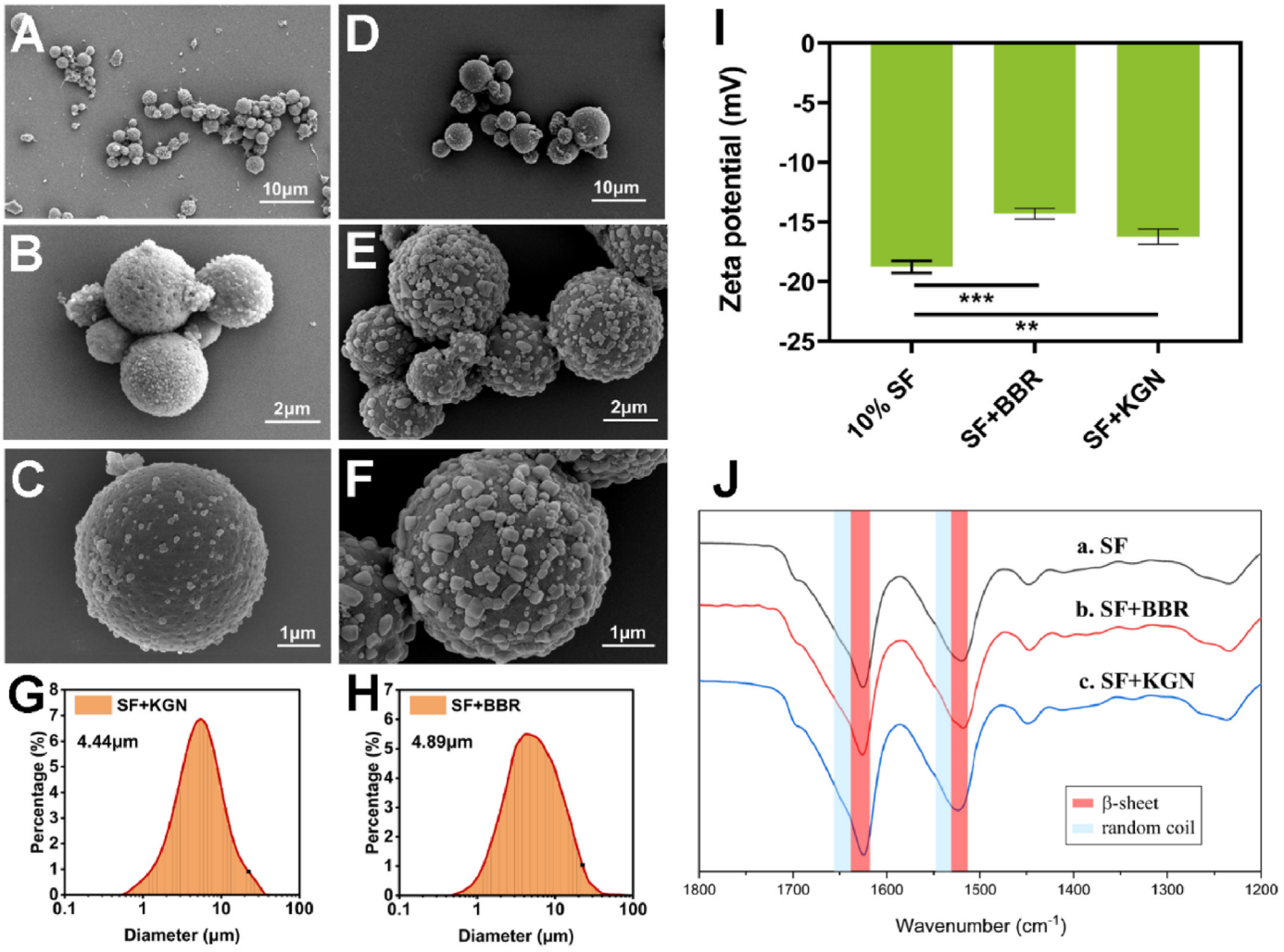

Fig. 3. SEM images of the SF-KGN microspheres (A–C) and SF-BBR microspheres (D–F). DLS measurements for the SF-KGN microspheres (G) and SF-BBR microspheres (H). Zeta potential (I) and FTIR spectra (J) of the microspheres. **P < 0.01 and ***P < 0.001.

the pore structure of S + B/S + K and S + B + K + P hydrogel (Fig. 4A, D, G). In addition, there were lumps of various sizes in the hydrogel network of S + B/S + K and S + B + K + P hydrogel (Fig. 4B, E, H). Further observations of the quenched sections across the lumps revealed that plentiful microspheres were embedded in the network fibers of S + B/S + K and S + B + K + P hydrogel (Fig. 4C, F, I). Therefore, the drug release profiles of SilMA hydrogels incorporated with drug-loaded microspheres were theoretically distinct from those of drug-loaded hydrogels and drug-loaded microspheres. At first, microspheres scattering in the pore structure of hydrogels released drugs, which were further released into the surrounding environment with the swelling process of hydrogels. Meanwhile, drugs released from microspheres embedded in the network fibers of hydrogels were blocked by the hydrogels and would gradually release with the degradation process of the hydrogels.

The release profiles of KGN and BBR from SilMA + KGNms and SilMA + BBRms hydrogels, respectively, confirmed the hypothesis above (Fig. 4J and K). In the first 30 days, the drug burst releases of microsphere-loaded hydrogels were significantly reduced and the release rates were slower, compared to those of drug-loaded hydrogels. The microsphere-loaded hydrogels showed an acceleration in drug release from about day 40 to the end of *in vitro* release studies at day 90. This two-stage release pattern may perfectly match the feature of cell-free scaffolds for tissue repair. In the early stage of implantation, there were only a small number of cells around the scaffold, the drug release was smooth to avoid causing cytotoxicity. As more cells were recruited into the scaffold for corresponding proliferation, differentiation and reconstruction, the scaffold gradually degraded to give up space and released more signaling molecules to regulate the cell differentiation.

The swelling ratio of S hydrogels was similar to that of S + B + K + P hydrogels, but lower than that of S + P hydrogels and higher than that of S + B + K hydrogels (Fig. 4L). The compressive elastic modulus of S hydrogels was similar to that of S + B + K + P hydrogels, but higher than that of S + P hydrogels and lower than that of S + B + K hydrogels (Fig. 4M). The *in vitro* degradation rate of S hydrogels was similar to that of S + B + K + P hydrogels, but slower than that of S + P hydrogels and faster than that of S + B + K hydrogels (Fig. 4N). The changes in the physical properties of S + P hydrogels were speculated to be attributed to the direct mixing of PRP and SilMA solution, which is equivalent to diluting the concentration of SilMA in hydrogels. A lower concentration of SilMA leads to a higher swelling ratio, lower compressive elastic modulus and faster *in vitro* degradation of the hydrogel, which is consistent with the previous results (Fig. 2D–F). The changes in the physical properties of S + B + K hydrogels were speculated to be attributed to the incorporation of SF microspheres. S + B + K hydrogel had the same concentration of SilMA as S hydrogel, but the incorporated SF microspheres were barely swelling and hard to be compressed and degraded due to their dense structure. The physical properties of S + B + K + P hydrogels were similar to those of S hydrogels, which was speculated to be attributed to the counteraction of both the influences caused by PRP and SF microspheres addition.

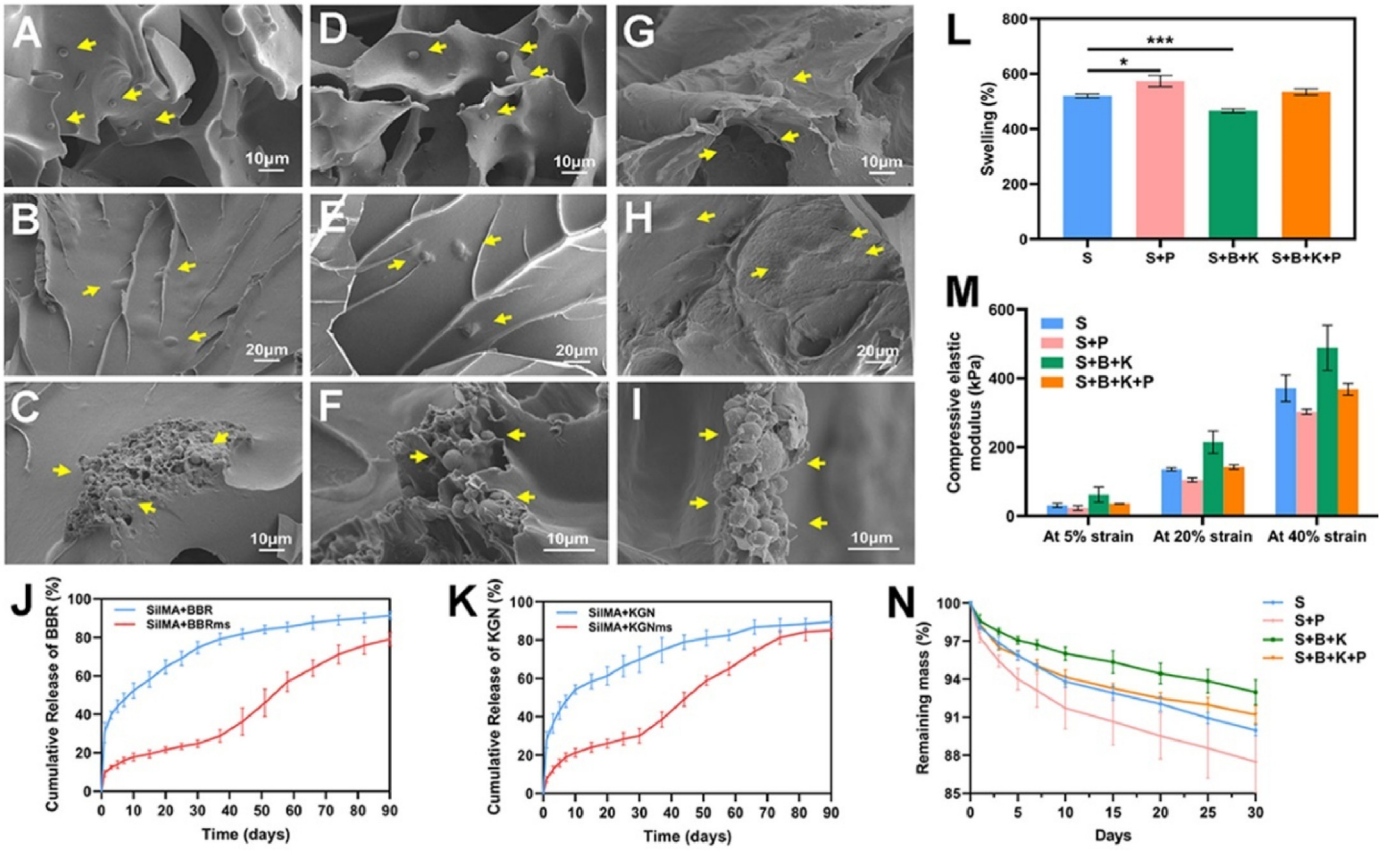

Fig. 4. Characterization of the composite bilayer SilMA hydrogels. SEM images of the S + B hydrogel (A–C), S + K hydrogel (D–F) and S + B + K + P hydrogel (G–I). Cumulative BBR release from SilMA + BBR and SilMA + BBRms hydrogels (J). Cumulative KGN release from SilMA + KGN and SilMA + KGNms hydrogels (K). Swelling ratio (L), compressive elastic modulus (M) and *in vitro* degradation profile (N) of the S, S + P, S + B + K and S + B + K + P hydrogels. *P < 0.05 and ***P < 0.001.

The biocompatibility of scaffolds is crucial for their application in tissue engineering. CCK-8 analysis showed that the cell proliferation rates increased over time on all hydrogels (Fig. S4). *In vivo* subcutaneous implantation also confirmed the good biocompatibility of all hydrogels (Fig. 5). M&T staining showed that no obvious layer of inflammatory cells was found around all hydrogels (Fig. 5A–D). H&E staining also observed that only a few inflammatory cells infiltrated in the surrounding tissues (Fig. 5E–H), confirming that all the hydrogels only caused a slight inflammatory reaction at 2 weeks post-implantation. After 2 weeks of subcutaneous implantation, hydrogels with PRP incorporation showed more fragmentations and more cells migrating into the hydrogels (Fig. 5J, L).

3.3. PRP promoted the migration of BMSCs in vitro

PRP can be easily obtained by collecting peripheral blood in a low invasive way. Therefore, the incorporation of PRP for promoting BMSCs migration will not hinder the clinical translation of the scaffold. Transwell assay results indicated that BMSCs migration was significantly promoted in medium containing low concentrations of PRP (1% and 5% vs. control) (Fig. S5). When PRP was incorporated into SilMA hydrogel, the number of migrating cells increased with the increase of PRP concentration from 1% to 20%, but the significance among groups decreased gradually (Fig. 6A–F). Theoretically, the implantation of S+20 P hydrogel can recruit the most cells. However, the strength of mechanical properties of hydrogel would reduce with the increase of PRP concentration. We have detected that the compressive elastic modulus of S+10 P hydrogel loading with SF microspheres (S + B + K + P hydrogel) was similar to that of S hydrogel (Fig. 4M). Thus, S+10 P (hereafter referred to as S + P) hydrogel was selected in this study for subsequent research in order to balance the conflicting needs between promoting cell migration and maintaining the high mechanical strength of hydrogel. Under the same conditions, the numbers of migrating cells were similar in the SilMA, S + B and S + K hydrogel groups (Fig. 6A, H, I), indicating that BBR and KGN did not promote cell migration. Compared to S + B and S + K hydrogels, cell migration was significantly promoted by S + P, S + B + P and S + K + P hydrogels (Fig. 6G-L). However, cell migration was reduced in the S + B + P hydrogel group compared to the S + P hydrogel group (Fig. 6G). This may be related to the inhibition of cell migration by BBR. To our knowledge, there is no study investigating the effect of BBR on BMSCs migration, but it has been reported that BBR can inhibit the invasion of tumor cells [50]. Taken together, we consider that the promotion of cell migration induced by PRP is stronger than the inhibition induced by BBR, thus the recruitment of BMSCs of the scaffold layer simultaneously incorporated PRP and SF-BBR microspheres was still sufficient.

3.4. KGN promoted BMSCs chondrogenic differentiation in vitro

KGN has been reported to induce BMSCs chondrogenic differentiation without the disadvantages of growth factors such as instability, immunogenicity, and short half-life [23–26]. q-PCR results showed that KGN significantly up-regulated the gene expression of *Sox9*, *Acan* and *Col2a1* of BMSCs at the concentration of 10 μM without TGF-β addition (Figs. S6A–C), consistent with previous studies [23,24]. Similarly, the gene expressions of *Sox9*, *Acan* and *Col2a1* of BMSCs cultured on S + K hydrogel were significantly increased as compared to S hydrogel (Figs. S6D–F). WB results showed that compared with the S group, the

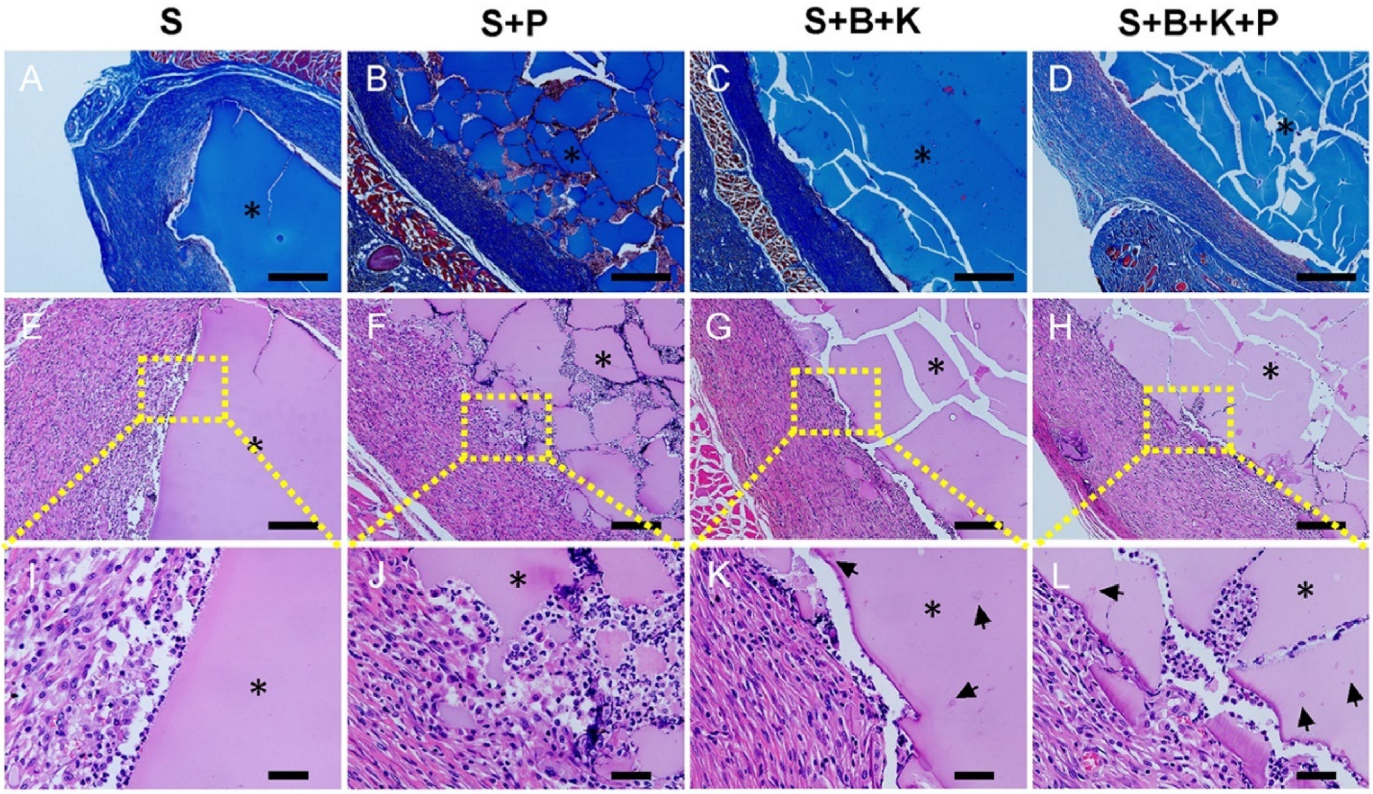

Fig. 5. Inflammatory response in tissues surrounding the subcutaneously implanted hydrogels. M&T staining of the S (A), S + P (B), S + B + K (C) and S + B + K + P (D) hydrogels. H&E staining of the S (E, I), S + P (F, J), S + B + K (G, K) and S + B + K + P (H, L) hydrogels. Scale bars = 600 μm in (A–D); Scale bars = 200 μm in (E–H); Scale bars = 40 μm in (I–L). * represents hydrogels; arrows represent drug-loaded SF microspheres.

expressions of COL2 and SOX9 in BMSCs were significantly up-regulated in S + K, S + P and S + K + P groups (Fig. 7C, I, J). The expression of SOX9 in the S + K + P group was significantly higher than that in S + K and S + P groups, and the expression of COL2 in the S + K + P group was significantly higher than that in the S + K group (Fig. 7C, I, J), suggesting that KGN and PRP play a synergistic role in promoting BMSCs chondrogenesis. GAG deposition was detected by Alcin blue staining, and it was observed that the S + K, S + P and S + K + P groups showed more intensive staining than the S group, while the S + K + P group revealed the most intensive staining (Fig. 7A).

3.5. BBR promoted BMSCs osteogenic differentiation in vitro

BBR has been widely studied due to its anti-inflammatory, antioxidant, antibacterial and immune regulation properties [51–53]. Recent studies have shown that BBR can promote the osteogenesis of BMSCs [27,28,32]. Similar to KGN, the stable molecular structure of BBR facilitates *in vitro* manipulation and encapsulation by various materials and maintains biological activity in the control release process. q-PCR results showed that the gene expression of *Alp, Bmp2*, *Runx2* and *Ocn* were gradually up-regulated with the increase of BBR concentration from 1 μM to 10 μM (Figs. S7E–H). The BMSCs treated with 10 μM BBR showed the highest osteogenic gene expression levels and the most intensive ALP staining (Figs. S7A–H). Since the molecular weight, effective concentration for inducing BMSCs differentiation, drug loading rate and release profiles on SF microspheres of BBR were similar to those of KGN, the loading amounts of SF-BBR microspheres on the subchondral bone layer could be the same as that of SF-KGN microspheres on the cartilage layer. Gene expressions of *Alp, Bmp2*, *Runx2* and *Ocn* of BMSCs cultured on S + B hydrogel were significantly increased as compared to S hydrogel (Fig. S7K-N). Likewise, the ALP staining was more intensive on S + B hydrogel than S hydrogel (Figs. S7I and J). WB results showed that compared with the S group, the expressions of RUNX2 and OPN in BMSCs were significantly up-regulated in S + B, S + P and S + B + P groups (Fig. 7G, M, N). The expressions of RUNX2 and OPN in the S + B + P group were higher than those in S + B and S + P groups, suggesting that BBR and PRP may play a synergistic role in promoting BMSCs osteogenesis (Fig. 7G, M, N). Similarly, it was observed that the S + B, S + P and S + B + P groups showed more intensive ALP staining than the S group, while the S + B + P group revealed the most intensive staining (Fig. 7E).

3.6. The composite scaffolds promoted the chondrogenesis and osteogenesis of BMSCs under inflammatory condition

It should be noted that the osteochondral engineering scaffolds are practically implanted in an environment with conditions harsher than the experimental conditions above. Firstly, a state of sterile inflammatory cascade exists in an injury joint with osteochondral defects. Moreover, the scaffold implantation surgery will further exacerbate the inflammatory state of the joint. Studies have shown that both the osteogenesis and chondrogenesis of BMSCs are significantly inhibited under inflammatory conditions [54,55]. Therefore, the evaluation of whether the composite scaffolds can promote BMSCs osteogenesis and chondrogenesis under inflammatory conditions is crucial. In this study, we used LPS to induce a cellular inflammatory microenvironment. After LPS treatment, the inflammatory cytokines, including TNF-α and IL-1β, produced by BMSCs were increased over time (Fig. S8).

The Alcin blue staining results and expression levels of COL2 and SOX9 were not significantly different between S and S + L groups (Fig. 6A, B, D, K, L). This may attribute to the absence of TGF-β in the chondrogenic conductive medium used in this study, leading to low levels of basic expression of COL2 and SOX9 in the S group. However, Alcin blue staining showed that the GAG deposition in S + K + L, S + P +

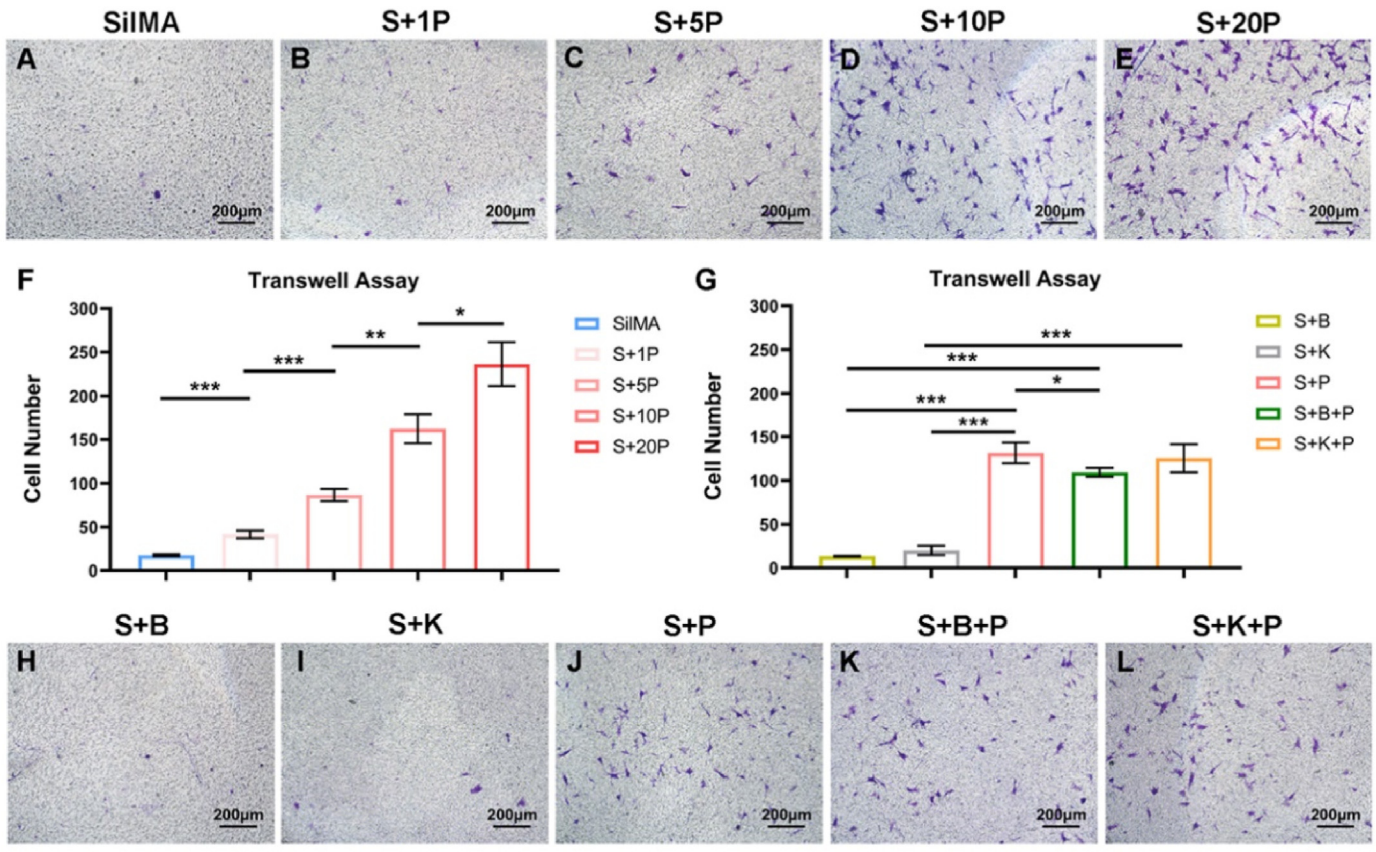

Fig. 6. Migration of BMSCs on different hydrogels. Transwell assay images of BMSCs cultivated on SilMA (A), S+1 P (B), S+5 P (C), S+10 P (D) and S+20 P (E) hydrogels. Quantification of cell number of migration for BMSCs cultivated on SilMA, S+1 P, S+5 P, S+10 P and S+20 P hydrogels (F). Quantification of cell number of migration for BMSCs cultivated on S + B, S + K, S + P, S + B + P and S + K + P hydrogels (G). Transwell assay images of BMSCs cultivated on S + B (H), S + K (I), S + P (J), S + B + P (K) and S + K + P (L) hydrogels. *P < 0.05, **P < 0.01 and ***P < 0.001.

L and S + K + P + L groups were respectively less than those in S + K, S + P and S + K + P groups (Fig. 7A and B), indicating that the chondrogenic differentiation of BMSCs was inhibited under inflammation. When comparing to the S + L group, the expressions of COL2 and SOX9 were significantly up-regulated and the Alcin blue staining was more intensive in S + K + L, S + P + L, S + K + P + L group (Fig. 7B, D, K, L), indicating that the composite scaffolds can promote BMSCs chondrogenesis under inflammation.

Compared to the S group, WB results showed that the expression of RUNX2 was significantly reduced and ALP staining results also showed that the expression of ALP was decreased in the S + L group (Fig. 7E, F, H, O), indicating that the osteogenic differentiation of BMSCs was significantly inhibited under inflammation. However, the expression of OPN showed no reduction with the addition of LPS (Fig. 7H, P). This may be because OPN has an anti-inflammatory property through the inhibition of inducible nitric oxide synthase (iNOS) [56]. The up-regulation of OPN expression may be part of the self-protection mechanism of BMSCs under inflammation. When comparing to the S + L group, WB results showed that the expressions of RUNX2 and OPN were significantly up-regulated and the ALP staining results also showed that the expression of ALP was increased in S + B + L, S + P + L, S + B + P + L group (Fig. 7E, F, H, O, P), indicating that the composite scaffolds can promote BMSCs osteogenesis under inflammation.

3.7. Osteochondral engineering using the all-silk-derived composite scaffolds

The S hydrogel functioned as the basic provisional matrix for tissue regeneration, mimicking the matrix stiffness of both cartilage and subchondral bone. The S + P hydrogel promoted the migration and predifferentiation of endogenous cells on the basis of the physical cues mentioned above. The S + B + K hydrogel realized the spatial control of the release of signal molecules. The S + B + K + P hydrogel, which integrated all physical and biochemical clues mentioned above, was expected to realize rapid endogenous cells recruitment at the early stage of implantation and promote the chondrogenesis and osteogenesis of BMSCs throughout the whole osteochondral regeneration period. All the hydrogel scaffolds were respectively implanted into rat osteochondral defects on the patellar groove to investigate the *in situ* therapeutic efficacy. After 4 weeks, macroscopic images revealed that the surface of the defect was covered by a layer of white and subtranslucent soft tissue in the S + B + K + P group, though the notch of the defect remained obvious (Fig. 8A). On the contrary, samples in the other 3 groups exhibited large defects in the central region (Fig. 8A). After 8 weeks, the smooth and flat cartilage-like tissue was completely covered the defect area with well integration with surrounding tissues in the S + B + K + P group (Fig. 8B). In S + P and S + B + K groups, the newly-formed cartilage-like tissues covered most of the defect area, while rare signs of tissue repair were found in the S group (Fig. 8B). Consequently, the ICRS macroscopic scores showed that the regeneration of cartilage in the S + B + K + P group was significantly better than that of the S group at week 4 post-implantation, and was significantly better than that of the other 3 groups at week 8 post-implantation (Fig. 8C).

The regenerations of subchondral bone at different times were evaluated by micro-CT reconstruction images. After 4 weeks, a huge subchondral bone defect remained in the S group; while small amounts of neo-bone were found in the other three groups (Fig. 8A). After 8 weeks, a few neo-bones were found in the S group, while the mature

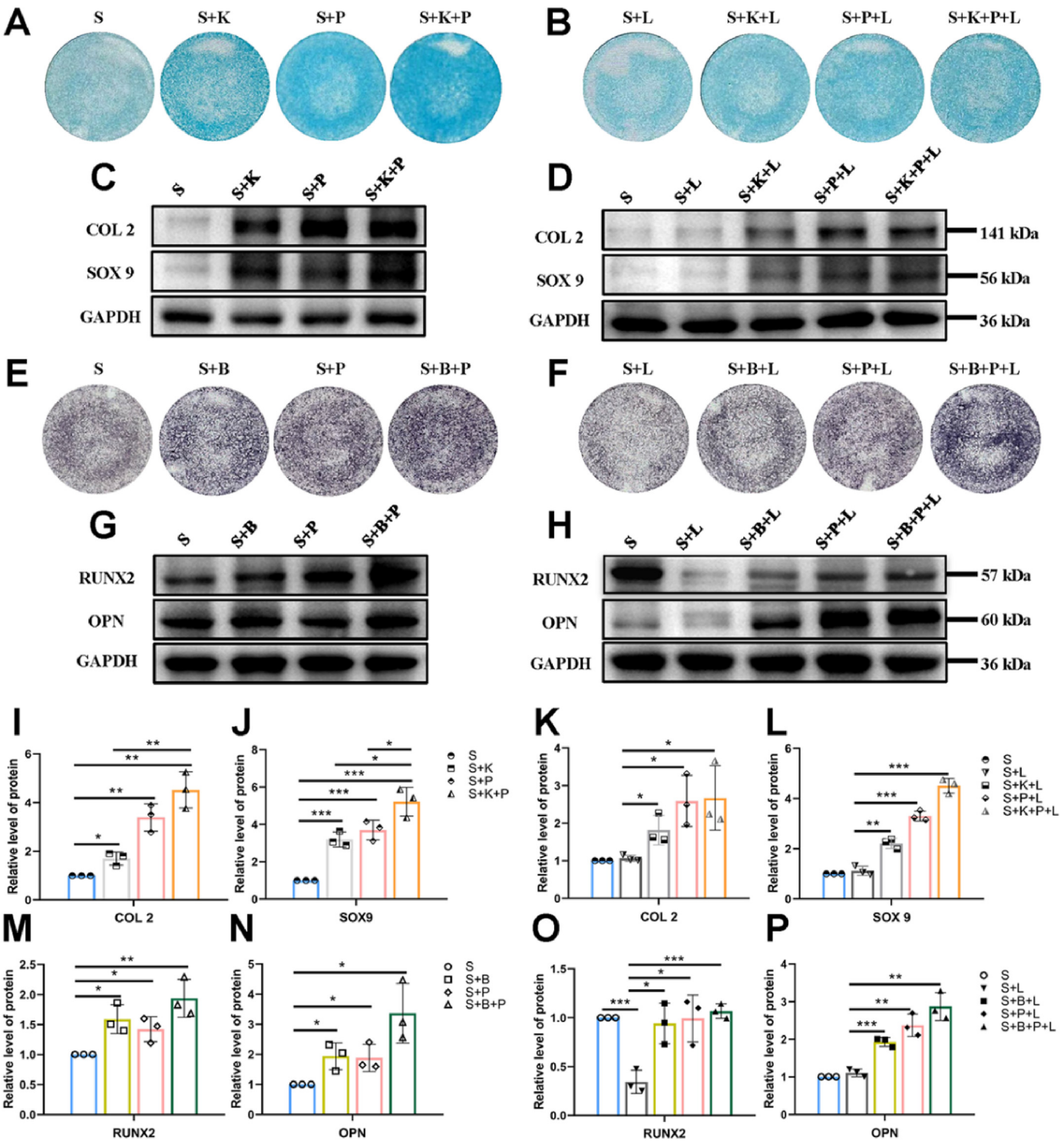

Fig. 7. Effect of composite hydrogels on inducing BMSCs chondrogenic and osteogenic differentiation under the normal condition and the inflammatory condition induced by LPS. Alcin blue staining results of Group S, S + K, S + P and S + K + P (A), and Group S + L, S + K + L, S + P + L and S + K + P + L (B). COL2 and SOX9 expression of BMSCs after inducing chondrogenic differentiation under the normal condition (C, I, J) and under the inflammation condition (D, K, L). ALP staining results of Group S, S + B, S + P and S + B + P (E), and Group S + L, S + B + L, S + P + L and S + B + P + L (F). RUNX2 and OPN expression of BMSCs after inducing osteogenic differentiation under the normal condition (G, M, N) and under the inflammation condition (H, O, P). *P < 0.05, **P < 0.01 and ***P < 0.001. (For interpretation of the references to colour in this figure legend, the reader is referred to the Web version of this article.)

bones almost fully filled the defect in the S + B + K + P group (Fig. 8B). In S + P and S + B + K groups, large amounts of neo-bones were found, but remained various sizes of void spaces yet to be regenerated (Fig. 8B). Through the quantification of bone formation, the BMD and BV/TV in S + P, S + B + K and S + B + K + P groups were significantly higher than those in the S group at both week 4 and week 8 of implantation (Fig. 8C and D). Similar results were shown in Tb. N, excepting that of S + B + K group compared with S group at week 8 of implantation (P = 0.0589) (Fig. 8E). These results indicated that the incorporation of PRP and SF-BBR microspheres can significantly promote the regeneration of

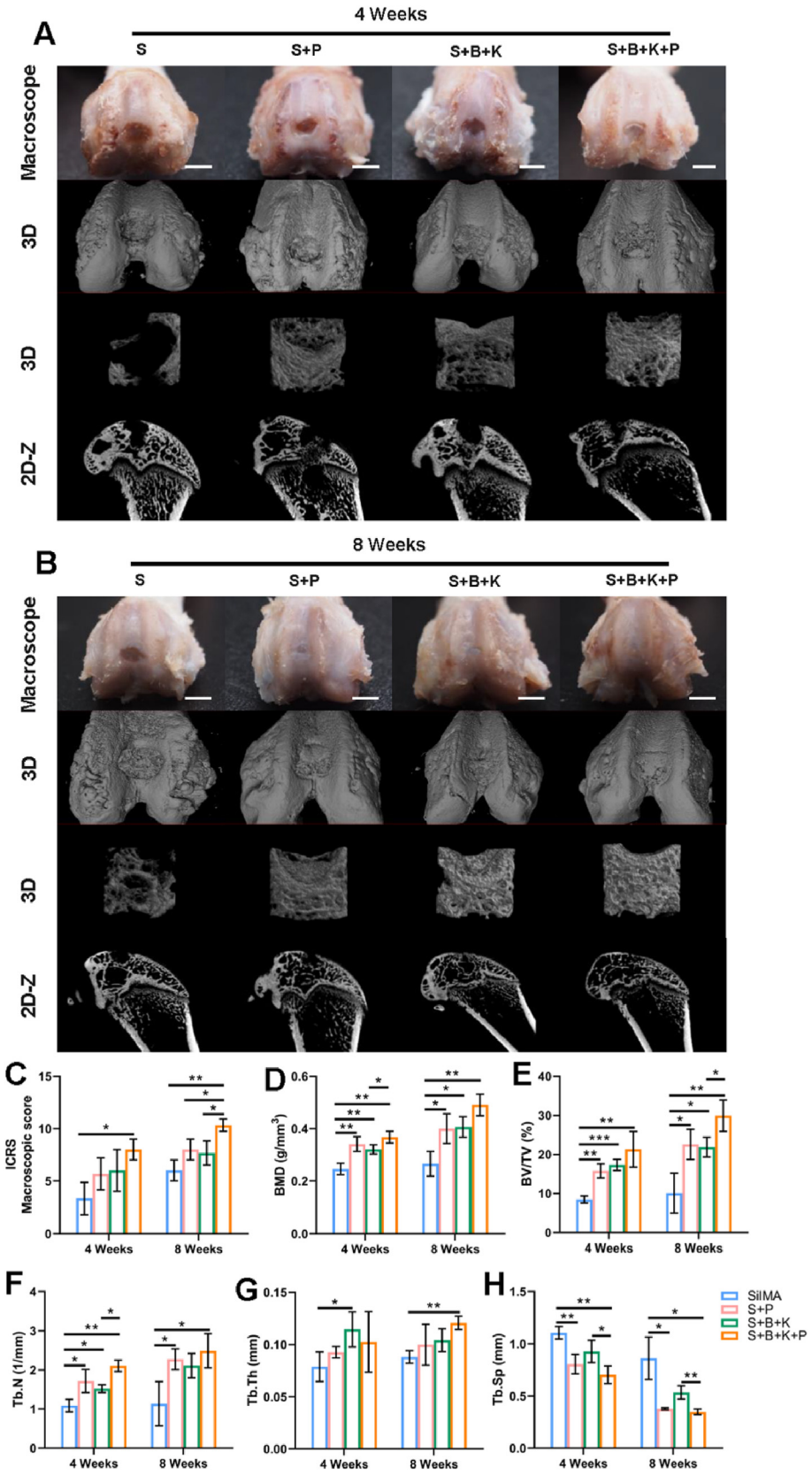

Fig. 8. Macroscopic and micro-CT observation of osteochondral repair using different hydrogel scaffolds. Macroscopic and micro-CT observation after 4 weeks (A) and 8 weeks (B) of implantation. (C) Macroscopic evaluation according to the ICRS macroscopic scores. Quantitation of BMD (D), BV/TV (E), Tb. N (F), Tb. Th (G) and Tb. Sp (H). Scale bar = 2 mm in (A, B). *P < 0.05, **P < 0.01 and ***P < 0.001.

subchondral bone. The S + B + K + P group had the highest values of BMD, BV/TV, Tb. N and Tb. Th and the lowest values of Tb. Sp among the 4 groups at week 8 (Fig. 8C–G). Taken together, the coexistence of PRP and BBR could further optimize the structure of new-formed trabecular bone.

Histological assessment of osteochondral regeneration was evaluated using H&E and Saf-O staining. After 4 weeks, the internal structure of S and S + B + K hydrogels remained intact, while various degrees of fragmentation were found in both S + P and S + B + K + P hydrogels (Fig. 9A), which provided space for endogenous cell migration. Cartilage-like and fibrous tissue began to appear and cover the surface of defects in S + P, S + B + K and S + B + K + P groups, while only disordered fibrous tissue was found on the surface of the S group (Fig. 9A). After 8 weeks, residual hydrogels were still found in S and S + B + K groups (Fig. 9B). Osteochondral regeneration with the correct formation of both cartilage and subchondral bone tissues was found in all groups, except the S group, whose defect region was still filled with disorder fibrous tissue (Fig. 9B). In the S + P group, the regenerated cartilage was thin and less smooth;

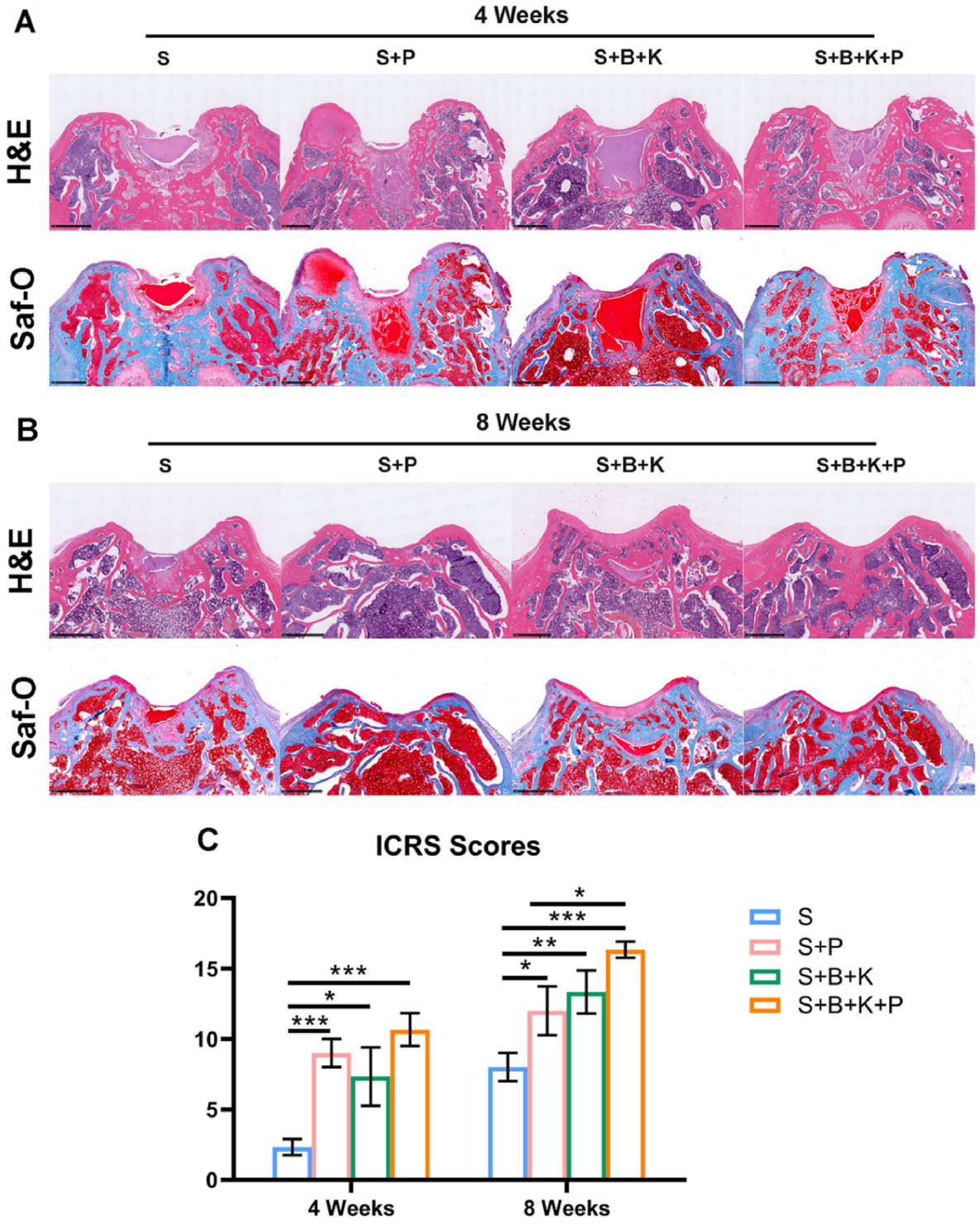

Fig. 9. Histological staining result of osteochondral repair using different hydrogel scaffolds. H&E staining and Saf-O staining results after 4 weeks (A) and 8 weeks (B) of implantation. (C) Quantitation of ICRS scores. Scale bar = 400 μm in (A, B). *P < 0.05, **P < 0.01 and ***P < 0.001.

and the structure of subchondral bone was sparse. In the S + B + K group, the regenerated cartilage was smooth and thick, but the deposition of the cartilage matrix was poor; and there was dense and thick subchondral bone tissue formed around the residual hydrogel. In the S + B + K + P group, the regenerated cartilage was smooth, and its thickness and matrix deposition were similar to adjacent natural cartilage tissue; and the subchondral bone was almost completely regenerated with total degradation of the hydrogel scaffold (Fig. 9B). Consequently, the ICRS scores showed that the regenerations of cartilage in the S + P, S + B + K and S + B + K + P groups were significantly better than that of the S group, and the S + B + K + P group had the highest score both at week 4 and week 8 post-implantation (Fig. 9C).

At 4 weeks post-implantation, immunohistochemical staining of Collagen II showed that the neo-tissue in the cartilage area was more strongly positive in the S + P, S + B + K and S + B + K + P groups, as compared to the S group (Fig. 10A). After 8 weeks, immunohistochemical staining displayed the most intense Collagen II staining in the repaired tissue from the S + B + K + P group, followed by the S + B + K group (Fig. 10B), in line with the results of H&E and Saf-O staining. At 4 weeks post-implantation, the repaired tissue in the S + P and S + B + K + P groups displayed higher proportion of CD44-positive cells as compared to the S and S + B + K groups, indicating that the incorporation of PRP could more efficiently recruit the endogenous BMSCs, which were defined as $CD44^{-}$, $CD90^{-}$and CD105-positive cells (Fig. 10C) [57]. After

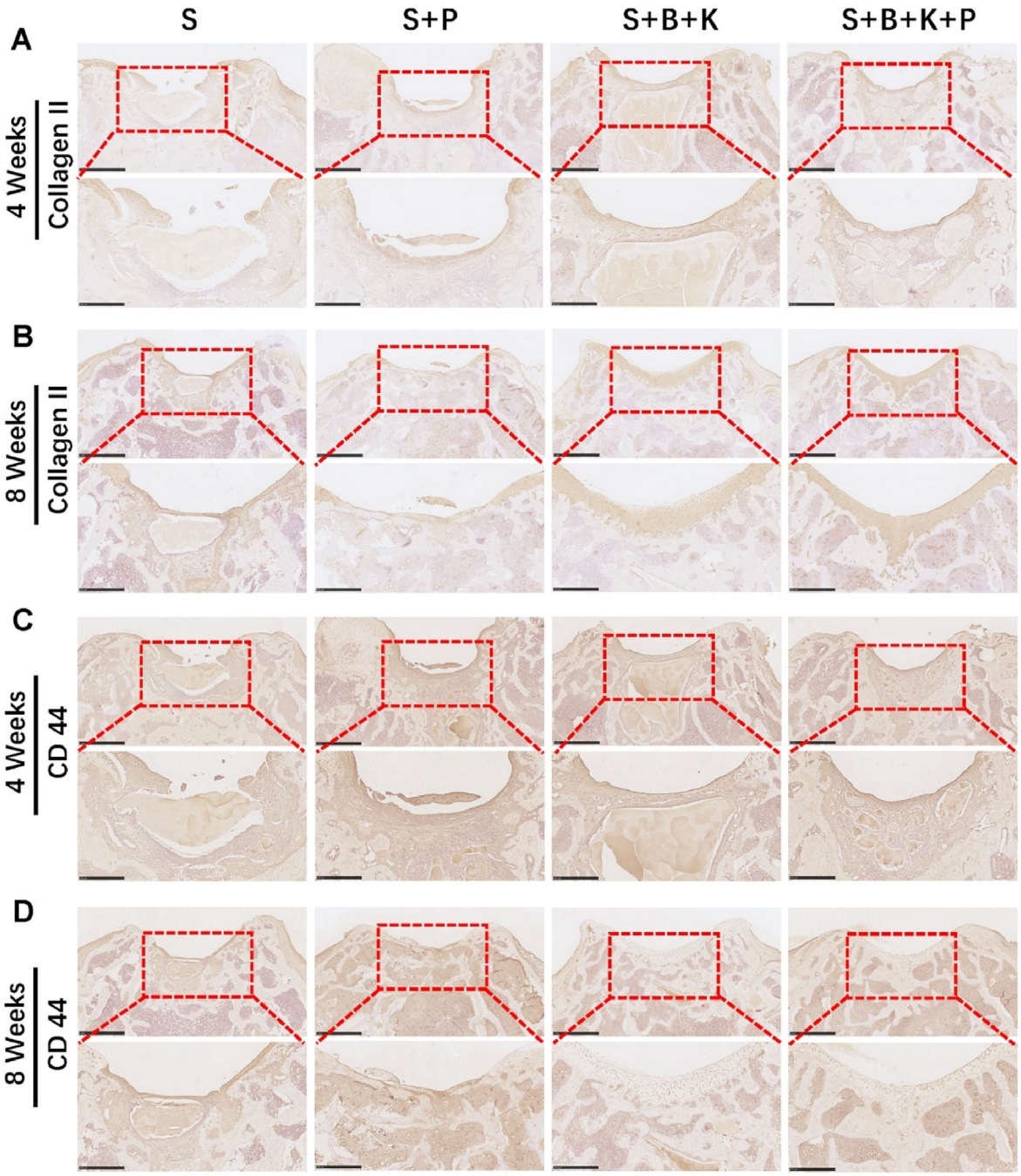

Fig. 10. Immunohistochemical staining result of osteochondral repair using different hydrogel scaffolds. Immunohistochemical staining for Collagen II of the repaired osteochondral tissue after 4 weeks (A) and 8 weeks (B) of implantation. Immunohistochemical staining for CD44 of the repaired osteochondral tissue after 4 weeks (C) and 8 weeks (D) of implantation. The lower panels represent higher magnification images of the corresponding red boxes in the upper panel. Scale bar = 1 mm in the upper panel and 500 μm in the lower panel. (For interpretation of the references to colour in this figure legend, the reader is referred to the Web version of this article.)

8 weeks, since the osteochondral defect was mostly regenerated, the number of CD44-positive cells was significantly reduced in the S + B + K and S + B + K + P groups; while there were still clusters of CD-44 positive cells in the S and S + P groups with relatively poor repair of the cartilage layer (Fig. 10D).

After 8 weeks of implantation, the hydrogel scaffolds were largely or completely degraded and the loaded biomolecules were released in large quantities. We therefore investigated whether the scaffold degradation products and the biomolecules released could damage important organs in the body during the metabolic process. No abnormality was observed in the heart, liver, spleen, lung and kidney tissue sections of all the experimental groups at week 8 after implantation, compared to those of the normal SD rats (Fig. S9). The above results indicated that S + B + K + P hydrogel exhibited optimal osteochondral defect repair with good biocompatibility after 8 weeks of implantation.

4. Conclusions

In summary, an all-silk-derived multifunctional biomaterial platform was constructed for osteochondral engineering. The integral stratified SilMA hydrogel scaffolds mimicked the gradient of matrix stiffness of osteochondral tissue. PRP incorporation reinforced the property of SilMA hydrogel in endogenous BMSCs migration and pre-differentiation at the early stage of implantation. The long-term regulations of BMSCs differentiation and tissue regeneration were realized by the stratified anchoring of the SF-KGN and SF-BBR microspheres. All the spatial and temporal control of biological cues conducive to osteochondral tissue regeneration were efficiently integrated through a simple process. Based on our findings, this composite has been demonstrated to realize satisfied cartilage and subchondral bone regeneration with great biocompatibility after 8 weeks of implantation. It is worthy of further investigation on this promising biomaterial platform and its clinical potential for osteochondral regeneration.

Credit author statement

Weizhou Jiang: Conceptualization, Methodology, Writing – original draft. Xiuting Xiang: Formal analysis, Data curation, Writing – review & editing. Minkai Song: Software, Visualization. Jianlin Shen: Software, Visualization. Zhanjun Shi: Supervision, Resources, Writing – review & editing. Wenhua Huang: Funding acquisition, Conceptualization, Writing – review & editing. Huan Liu: Funding acquisition, Conceptualization, Resources, Writing – review & editing.

Declaration of competing interest

The authors declare that they have no known competing financial interests or personal relationships that could have appeared to influence the work reported in this paper.

Data availability

Data will be made available on request.

Acknowledgements

This work was funded by the National Natural Science Foundation of China (31972915), Guangdong Basic and Applied Basic Research Foundation (2020B1515120001), Science and Technology Project of Putian City (2060499 to JS), Sichuan Applied Basic Research Project (2018JY0402) and Technology Strategic Cooperation Project of Southwest Medical University Science and Luzhou (2018LZXNYD-ZK19). The authors gratefully acknowledge Prof. Xiaoqin Wang and Dr. Jianbing Wu at Soochow University for their assistance on the fabrication and characterization of silk fibroin nano- and microspheres.

Appendix A. Supplementary data

Supplementary data to this article can be found online at https://doi.org/10.1016/j.mtbio.2022.100485.

References

[1] D.J. Huey, J.C. Hu, K.A. Athanasiou, Unlike bone, cartilage regeneration remains elusive, Science 338 (2012) 917–921.
[2] H. Kwon, W.E. Brown, C.A. Lee, D. Wang, N. Paschos, J.C. Hu, et al., Surgical and tissue engineering strategies for articular cartilage and meniscus repair, Nat. Rev. Rheumatol. 15 (2019) 550–570.
[3] P.C. Kreuz, M.R. Steinwachs, C. Erggelet, S.J. Krause, G. Konrad, M. Uhl, et al., Results after microfracture of full-thickness chondral defects in different compartments in the knee, Osteoarthritis Cartilage 14 (2006) 1119–1125.
[4] H.S. Vasiliadis, B. Danielson, M. Ljungberg, B. McKeon, A. Lindahl, L. Peterson, Autologous chondrocyte implantation in cartilage lesions of the knee: long-term evaluation with magnetic resonance imaging and delayed gadolinium-enhanced magnetic resonance imaging technique, Am. J. Sports Med. 38 (2010) 943–949.
[5] L. Peterson, H.S. Vasiliadis, M. Brittberg, A. Lindahl, Autologous chondrocyte implantation: a long-term follow-up, Am. J. Sports Med. 38 (2010) 1117–1124.
[6] M. Marcacci, G. Filardo, E. Kon, Treatment of cartilage lesions: what works and why? Injury 44 (Suppl 1) (2013) S11–S15.
[7] S. Glyn-Jones, A.J. Palmer, R. Agricola, A.J. Price, T.L. Vincent, H. Weinans, et al., Osteoarthritis, Lancet (London, England) 386 (2015) 376–387.
[8] regional Global, and national disability-adjusted life-years (DALYs) for 333 diseases and injuries and healthy life expectancy (HALE) for 195 countries and territories, 1990-2016: a systematic analysis for the Global Burden of Disease Study 2016, Lancet (London, England) 390 (2017) 1260–1344.
[9] J.N. Fu, X. Wang, M. Yang, Y.R. Chen, J.Y. Zhang, R.H. Deng, et al., Scaffold-Based tissue engineering strategies for osteochondral repair, Front. Bioeng. Biotechnol. 9 (2021), 812383.
[10] K. Sadtler, A. Singh, M.T. Wolf, X. Wang, J.H. Elisseeff, Design, clinical translation and immunological response of biomaterials in regenerative medicine, Nat. Rev. Mater. 1 (2016), 16040.
[11] C. Li, L. Ouyang, J.P.K. Armstrong, M.M. Stevens, Advances in the fabrication of biomaterials for gradient tissue engineering, Trends Biotechnol. 39 (2021) 150–164.
[12] F.R. Maia, M.R. Carvalho, J.M. Oliveira, R.L. Reis, Tissue engineering strategies for osteochondral repair, Adv. Exp. Med. Biol. 1059 (2018) 353–371.
[13] J. Farr, G.C. Gracitelli, N. Shah, E.Y. Chang, A.H. Gomoll, High failure rate of a decellularized osteochondral allograft for the treatment of cartilage lesions, Am. J. Sports Med. 44 (2016) 2015–2022.
[14] M. Brix, M. Kaipel, R. Kellner, M. Schreiner, S. Apprich, H. Boszotta, et al., Successful osteoconduction but limited cartilage tissue quality following osteochondral repair by a cell-free multilayered nano-composite scaffold at the knee, Int. Orthop. 40 (2016) 625–632.
[15] A. Azam, M. Forster, A. Robertson, Clinical and radiological outcome for Trufit Plug in the treatment of chondral and osteochondral lesions at a minimum of 2 years, J. Orthop. 15 (2018) 47–51.
[16] V.P. Ribeiro, S. Pina, J.M. Oliveira, R.L. Reis, Silk fibroin-based hydrogels and scaffolds for osteochondral repair and regeneration, Adv. Exp. Med. Biol. 1058 (2018) 305–325.
[17] P. Bhattacharjee, B. Kundu, D. Naskar, H.W. Kim, T.K. Maiti, D. Bhattacharya, et al., Silk scaffolds in bone tissue engineering: an overview, Acta Biomater. 63 (2017) 1–17.
[18] S.H. Kim, Y.K. Yeon, J.M. Lee, J.R. Chao, Y.J. Lee, Y.B. Seo, et al., Precisely printable and biocompatible silk fibroin bioink for digital light processing 3D printing, Nat. Commun. 9 (2018) 1620.
[19] S.H. Kim, D.Y. Kim, T.H. Lim, C.H. Park, Silk fibroin bioinks for digital light processing (DLP) 3D bioprinting, Adv. Exp. Med. Biol. 1249 (2020) 53–66.
[20] H. Hong, Y.B. Seo, D.Y. Kim, J.S. Lee, Y.J. Lee, H. Lee, et al., Digital light processing 3D printed silk fibroin hydrogel for cartilage tissue engineering, Biomaterials 232 (2020), 119679.
[21] X. Wu, M. Zhou, F. Jiang, S. Yin, S. Lin, G. Yang, et al., Marginal sealing around integral bilayer scaffolds for repairing osteochondral defects based on photocurable silk hydrogels, Bioact. Mater. 6 (2021) 3976–3986.
[22] P. Everts, K. Onishi, P. Jayaram, J.F. Lana, K. Mautner, Platelet-rich plasma: new performance understandings and therapeutic considerations in 2020, Int. J. Mol. Sci. (2020) 21.
[23] K. Johnson, S. Zhu, M.S. Tremblay, J.N. Payette, J. Wang, L.C. Bouchez, et al., A stem cell-based approach to cartilage repair, Science 336 (2012) 717–721.
[24] G. Cai, W. Liu, Y. He, J. Huang, L. Duan, J. Xiong, et al., Recent advances in kartogenin for cartilage regeneration, J. Drug Target. 27 (2019) 28–32.
[25] X. Liu, Y. Chen, A.S. Mao, C. Xuan, Z. Wang, H. Gao, et al., Molecular recognition-directed site-specific release of stem cell differentiation inducers for enhanced joint repair, Biomaterials 232 (2020), 119644.
[26] H. Xuan, H. Hu, C. Geng, J. Song, Y. Shen, D. Lei, et al., Biofunctionalized chondrogenic shape-memory ternary scaffolds for efficient cell-free cartilage regeneration, Acta Biomater. 105 (2020) 97–110.
[27] S. Mahya, J. Ai, S. Shojae, H.A. Khonakdar, G. Darbemamieh, S. Shirian, Berberine loaded chitosan nanoparticles encapsulated in polysaccharide-based hydrogel for the repair of spinal cord, Int. J. Biol. Macromol. 182 (2021) 82–90.

[28] P. Chen, C. Xia, J. Mo, S. Mei, X. Lin, S. Fan, Interpenetrating polymer network scaffold of sodium hyaluronate and sodium alginate combined with berberine for osteochondral defect regeneration, Materials science & engineering C, Materials for biological applications 91 (2018) 190–200.
[29] Y. Zhou, S.Q. Liu, L. Yu, B. He, S.H. Wu, Q. Zhao, et al., Berberine prevents nitric oxide-induced rat chondrocyte apoptosis and cartilage degeneration in a rat osteoarthritis model via AMPK and p38 MAPK signaling, Apoptosis : an international journal on programmed cell death 20 (2015) 1187–1199.
[30] P.F. Hu, W.P. Chen, J.L. Tang, J.P. Bao, L.D. Wu, Protective effects of berberine in an experimental rat osteoarthritis model, Phytother Res. : PT 25 (2011) 878–885.
[31] W. Li, Y. Liu, B. Wang, Y. Luo, N. Hu, D. Chen, et al., Protective effect of berberine against oxidative stress-induced apoptosis in rat bone marrow-derived mesenchymal stem cells, Exp. Ther. Med. 12 (2016) 4041–4048.
[32] R. Zhou, F. Chen, H. Liu, X. Zhu, X. Wen, F. Yu, et al., Berberine ameliorates the LPS-induced imbalance of osteogenic and adipogenic differentiation in rat bone marrow-derived mesenchymal stem cells, Mol. Med. Rep. 23 (2021).
[33] J. Wu, Z. Zheng, G. Li, D.L. Kaplan, X. Wang, Control of silk microsphere formation using polyethylene glycol (PEG), Acta Biomater. 39 (2016) 156–168.
[34] H. Gong, J. Wang, J. Zhang, J. Wu, Z. Zheng, X. Xie, et al., Control of octreotide release from silk fibroin microspheres, Materials science & engineering C, Materials for biological applications 102 (2019) 820–828.
[35] D.N. Rockwood, R.C. Preda, T. Yücel, X. Wang, M.L. Lovett, D.L. Kaplan, Materials fabrication from Bombyx mori silk fibroin, Nat. Protoc. 6 (2011) 1612–1631.
[36] R. Landesberg, M. Roy, R.S. Glickman, Quantification of growth factor levels using a simplified method of platelet-rich plasma gel preparation, J. Oral Maxillofac. Surg. : official journal of the American Association of Oral and Maxillofacial Surgeons 58 (2000) 297–300, discussion -1.
[37] V. Chan, P. Zorlutuna, J.H. Jeong, H. Kong, R. Bashir, Three-dimensional photopatterning of hydrogels using stereolithography for long-term cell encapsulation, Lab Chip 10 (2010) 2062–2070.
[38] P. Mainil-Varlet, T. Aigner, M. Brittberg, P. Bullough, A. Hollander, E. Hunziker, et al., Histological assessment of cartilage repair: a report by the histology endpoint committee of the international cartilage repair society (ICRS), J. Bone Jt. Surg. Am. Vol. 85 (A Suppl 2) (2003) 45–57.
[39] M.P. van den Borne, N.J. Raijmakers, J. Vanlauwe, J. Victor, S.N. de Jong, J. Bellemans, et al., International cartilage repair society (ICRS) and oswestry macroscopic cartilage evaluation scores validated for use in autologous chondrocyte implantation (ACI) and microfracture, Osteoarthritis Cartilage 15 (2007) 1397–1402.
[40] Q. Liu, H. Liu, Y. Fan, Preparation of silk fibroin carriers for controlled release, Microsc. Res. Tech. 80 (2017) 312–320.
[41] A.J. Engler, S. Sen, H.L. Sweeney, D.E. Discher, Matrix elasticity directs stem cell lineage specification, Cell 126 (2006) 677–689.
[42] R. Nicolete, M. Lima Kde, J.M. Júnior, M.D. Baruffi, A.I. de Medeiros, M.V. Bentley, et al., In vitro and in vivo activities of leukotriene B4-loaded biodegradable microspheres, Prostag. Other Lipid Mediat. 83 (2007) 121–129.
[43] J.H. Park, H.E. Jin, D.D. Kim, S.J. Chung, W.S. Shim, C.K. Shim, Chitosan microspheres as an alveolar macrophage delivery system of ofloxacin via pulmonary inhalation, Int. J. Pharm. 441 (2013) 562–569.
[44] L.D. Koh, Y. Cheng, C.P. Teng, Y.W. Khin, X.J. Loh, S.Y. Tee, et al., Structures, mechanical properties and applications of silk fibroin materials, Prog. Polym. Sci. 46 (2015) 86–110.
[45] X. Wang, T. Yucel, Q. Lu, X. Hu, D.L. Kaplan, Silk nanospheres and microspheres from silk/pva blend films for drug delivery, Biomaterials 31 (2010) 1025–1035.
[46] L. Fang, H. Fan, C. Guo, L. Cui, P. Zhang, H. Mu, et al., Novel mitochondrial targeting multifunctional surface charge-reversal polymeric nanoparticles for cancer treatment, J. Biomed. Nanotechnol. 15 (2019) 2151–2163.
[47] R. Dhurat, M. Sukesh, Principles and methods of preparation of platelet-rich plasma: a review and author's perspective, J. Cutan. Aesthetic Surg. 7 (2014) 189–197.
[48] R.E. Marx, E.R. Carlson, R.M. Eichstaedt, S.R. Schimmele, J.E. Strauss, K.R. Georgeff, Platelet-rich plasma: growth factor enhancement for bone grafts, Oral Surg. Oral Med. Oral Pathol. Oral Radiol. Endod. 85 (1998) 638–646.
[49] W.S. Vanden Berg-Foels, In situ tissue regeneration: chemoattractants for endogenous stem cell recruitment. Tissue engineering Part B, Review 20 (2014) 28–39.
[50] H.W. Qi, L.Y. Xin, X. Xu, X.X. Ji, L.H. Fan, Epithelial-to-mesenchymal transition markers to predict response of Berberine in suppressing lung cancer invasion and metastasis, J. Transl. Med. 12 (2014) 22.
[51] J. Jin, M. Xu, Y. Liu, Z. Ji, K. Dai, L. Zhang, et al., Alginate-based composite microspheres coated by berberine simultaneously improve hemostatic and antibacterial efficacy, Colloids Surf., B 194 (2020), 111168.
[52] B. Cai, Q. Zou, Y. Zuo, Q. Mei, J. Ma, L. Lin, et al., Injectable gel constructs with regenerative and anti-infective dual effects based on assembled chitosan microspheres, ACS Appl. Mater. Interfaces 10 (2018) 25099–25112.
[53] S.M. Ehteshamfar, M. Akhbari, J.T. Afshari, M. Seyedi, B. Nikfar, Anti-inflammatory and Immune-Modulatory Impacts of Berberine on Activation of Autoreactive T Cells in Autoimmune Inflammation, vol. 24, 2020, pp. 13573–13588.
[54] S. Chen, H. Liang, Y. Ji, H. Kou, C. Zhang, G. Shang, et al., Curcumin modulates the crosstalk between macrophages and bone mesenchymal stem cells to ameliorate osteogenesis, Front. Cell Dev. Biol. 9 (2021), 634650.
[55] J. Zhu, H. Tang, Z. Zhang, Y. Zhang, C. Qiu, L. Zhang, et al., Kaempferol slows intervertebral disc degeneration by modifying LPS-induced osteogenesis/adipogenesis imbalance and inflammation response in BMSCs, Int. Immunopharm. 43 (2017) 236–242.
[56] A.S. Lamort, I. Giopanou, Osteopontin as a link between inflammation and cancer: the thorax in the spotlight, Cells 8 (2019).
[57] Z. Shao, X. Zhang, Y. Pi, X. Wang, Z. Jia, J. Zhu, et al., Polycaprolactone electrospun mesh conjugated with an MSC affinity peptide for MSC homing in vivo, Biomaterials 33 (2012) 3375–3387.